LNF-95/012

Study of the High Energy Cosmic Ray Cascades Using the Dual Parton Model

G. Battistoni, C. Forti, J. Ranft

Astroparticle Physics 3, 157-184, (1995)

ELSEVIER

Astroparticle Physics 3 (1995) 157–184

Astroparticle Physics

Study of the high energy cosmic ray cascades using the dual parton model

G. Battistoni [a,b], C. Forti [a], J. Ranft [a]

[a] *INFN, Laboratorio Nazionali di Frascati, I-00044 Frascati (Rome), Italy*

[b] *INFN, Sezione di Milano, I-20133 Milan, Italy*

Received 8 October 1994

Abstract

In this paper we describe an application of the two component dual parton model, for the simulation of high energy cosmic ray cascades. The DPMJET interaction model has been tuned to accelerator data for hadron–nucleus and nucleus–nucleus interactions, and its performance in the fragmentation region has been optimized. We make use of this generator inside the HEMAS shower code. Results are presented with particular emphasis on the electromagnetic component and on the high energy muon content of the showers.

1. Introduction

A hadron production model to be used at cosmic ray energies should take into account all possible information from fixed target and collider experiments at accelerators. There are however important differences: in order to study the cosmic ray cascade, the main interest is in the forward fragmentation region of hadron–nucleus and nucleus–nucleus collisions. At accelerators, the central region in hadron–hadron collisions is usually best studied.

In this paper we will discuss hadron production in the framework of the dual parton model with emphasis in the fragmentation region. Important for cosmic ray studies are two aspects of multiparticle production:

(i) The change of particle production with energy, starting from the region well studied at present accelerator experiments;

(ii) the dependence of particle production on the nuclear target (and projectile).

A model for hadronic and nuclear interactions to be used in cosmic ray physics should provide the basic hadronic interaction term for the cosmic ray cascade. It should provide the cross sections for hadron–hadron, hadron–nucleus and nucleus–nucleus collisions as a function of the energy. Secondary π^0 and η mesons are the main source of the electromagnetic shower, secondary $\pi^{\pm}$ and $K^{\pm}$ mesons are the main source of cosmic ray muons and of atmospheric Neutrinos produced by the cosmic ray cascade. Secondary charmed mesons are the source for prompt muons and neutrinos. The model should work from the pion production threshold up to the highest possible primary energies.

Soft multiparticle production characterizing hadronic interactions at supercollider or cosmic ray energies cannot be understood purely within theoretical approaches provided by perturbative QCD. The nonperturbative

SSDI 0927-6505(94)00039-5

soft component of hadron production, which is responsible for all of hadron production at low energies, is still acting at higher energies.

The dual parton model (DPM) (a recent review is given in Ref. [1]) has been very successfully describing soft hadronic processes. The code DPMJET-II (a more complete description is given in Ref. [2]) is an event generator for hadron–hadron, hadron–nucleus and nucleus–nucleus collisions written on the basis of the two-component dual parton model to be used in the cosmic ray cascade.

In Section 2 we give a short account of the dual parton model. The code used in this paper for the generation of the hadronic interactions (DPMJET-II) is illustrated in Section 3. Its features at high cosmic ray energies are reviewed in Section 4. Section 5 describes the main features of the shower simulation code HEMAS-DPM. The results for cosmic ray showers are shown in Section 6, where we also report a comparison with the calculations using the original HEMAS interaction model. A Summary is given in Section 7.

2. The dual parton model

2.1. The energy dependence of multiparticle production and the two-component dual parton model for hadron–hadron collisions

The two-component dual parton model used here has been described fully in Refs. [3,4].

The soft input cross section in our unitarization scheme is described by the supercritical pomeron

$$\sigma_s = g^2 s^{\alpha(0)-1} \tag{1}$$

with g being the effective proton–pomeron coupling constant, and $\alpha(0)$ the pomeron intercept. The corresponding pomeron-trajectory is given by $\alpha(t) = \alpha(0) + \alpha' t$. The supercritical pomeron was used in the two-component DPM from the beginning [5].

The input cross section for semihard multiparticle production σ_h is calculated applying the QCD improved parton model, the details are given in Refs. [5–8]:

$$\sigma_h = \sum_{i,j} \int_0^1 dx_1 \int_0^1 dx_2 \int d\hat{t}\, \frac{1}{1+\delta_{ij}} \frac{d\sigma_{QCD,ij}}{d\hat{t}}\, f_i(x_1, Q^2) f_j(x_2, Q^2) \Theta(p_\perp - p_{\perp thr}) \tag{2}$$

$f_i(x, Q^2)$ are the structure functions of partons with the flavor i and scale Q^2, and the sum i, j runs over all possible flavors. To remain in the region where perturbation theory is valid, we use a low $p_\perp$ cut-off, $p_{\perp_{thr}}$, for the minijet component. Furthermore, since we calculate $\sigma_{QCD,ij}$ in lowest-order QCD perturbation theory, we multiply the hard input cross section σ_h with a K factor in the range of 1.5 to 2.

The momentum fractions of the constituents at the ends of the different chains are sampled using the exclusive parton distribution, which has the form for an event with n_s soft and n_h ($n_h \geq 1$) hard pomerons

$$\rho(x_1, \ldots, x_{2n_s}, \ldots, x_{2n_s+2+n_h}) \sim \frac{1}{\sqrt{x_1}} \left(\prod_{i=3}^{2n_s+2} \frac{1}{\sqrt{x_i}} \right) x_2^{1.5} \prod_{i=2n_s+3}^{2n_s+2+n_h} g(x_i, Q_i)\, \delta\left(1 - \sum_{i=1}^{2n_s+2+n_h} x_i\right). \tag{3}$$

The distributions $g(x_i, Q_i)$ are the distribution functions of the partons engaged in the hard scattering. The Regge behaviour of the soft valence quark x-distributions is $x^{-0.5}$, and the term $1/\sqrt{x_1}$ refers to the valence quark at the end of a soft valence chain. The Regge behaviour of a diquark x-distribution is $x^{1.5}$, and the term $x_2^{1.5}$ refers to the x-distribution of the valence diquark at the end of a soft valence chain. The Regge behaviour of soft sea-quark x-distributions agrees with the one of the valence quarks, and it is also $x^{-0.5}$. The terms $1/\sqrt{x_i}$ refer to the sea-quarks and sea-antiquarks at the end of soft sea chains. Here one remark is necessary.

In the previous papers [3,4] we did use terms $1/x_i$ for the soft sea-quarks and antiquarks. A corresponding formula with $1/x_i$ is also given in the dual parton model review [1]. The use of this different behaviour for the soft sea-quark x-distributions was certainly motivated by the behaviour of the deep inelastic x-distributions for sea-quarks, but it is not correct for the soft sea quarks. The correct Regge behaviour of soft sea quarks was already discussed in an appendix to the paper of Capella and Tran Thanh Van [9] and it is also given for instance in [10]. It is easy to check that, at low energies typical for fixed target experiments, the use of the correct form $1/\sqrt{x}$, or of $1/x$ is not very important, the behaviour being mainly determined by the low x cut-off of the structure functions. But for our goal, to study the Feynman x_F distributions of hadrons at the highest energies in the fragmentation region, it is essential to use the correct form $1/\sqrt{x}$.

Soft (s), hard (h), high mass single diffractive (TP stands for "triple pomeron" graph), and high mass double diffractive (L stands for "loop" graph) processes are treated simultaneously within an eikonal unitarization scheme using the impact parameter representation

$$\chi_i(B,s) = \frac{\sigma_i(s)}{8\pi b_i}\exp\left[-\frac{B^2}{4b_i}\right], \quad i = s,h,TP,L \tag{4}$$

normalized by

$$\int 2\chi_i(B,s)\,d^2B = \sigma_i \tag{5}$$

with b_h energy independent, and $b_s = b_{TP} = b_L = b + \alpha' \log(s)$. The exclusive cross section for l_c cut soft pomerons, m_c cut hard pomerons, n_c cut triple-pomeron graphs and p_c cut loop graphs is given by

$$\sigma(l_c,m_c,n_c,p_c,B,s) = \frac{(2\chi_s)^{l_c}}{l_c!}\frac{(2\chi_h)^{m_c}}{m_c!}\frac{(-2\chi_{TP})^{n_c}}{n_c!}\frac{(-2\chi_L)^{p_c}}{p_c!}\exp[-2\chi(B,s)] \tag{6}$$

with

$$\chi(B,s) = \chi_s(B,s) + \chi_h(B,s) - \chi_{TP}(B,s) - \chi_L(B,s). \tag{7}$$

The total and elastic cross section are given by

$$\sigma_{tot} = 4\pi\int_0^\infty BdB(1-\exp[\chi(B,s)]), \quad \sigma_{el}(B,s) = \tfrac{1}{4}[\sigma_{tot}(B,s)]^2. \tag{8}$$

Diffractive processes characterized by the excitation of an initial hadron to intermediate resonances (low mass diffractive interactions) are introduced via a two channel eikonal formalism.

2.2. *The dual parton model for hadron production in hadron–nucleus and nucleus–nucleus collisions*

In the following, we shall briefly sketch the basic ideas of the model and mention the most important ingredients; for a more detailed description of the model as applied in the code we refer to Refs. [11–16].

2.2.1. *The Monte Carlo realization of the dual parton model DTUNUC for hadron–nucleus and nucleus–nucleus collisions*

The model starts from the impulse approximation for the interacting nuclei, i.e. with a frozen discrete spatial distribution of nucleons sampled from standard density distributions [17]. The primary interaction of the incident high-energy projectile proceeds totally via n elementary collisions between $n_p = n_A$ and $n_t = n_B$ nucleons from the projectile (for incident hadrons $n_p = 1$) and the target nuclei, respectively. Actual numbers n, n_p and n_t are sampled on the basis of Glauber's multiple scattering formalism using the Monte Carlo algorithm of Ref.

[17]. Note that individual hadrons may undergo several interactions. Particle production in each elementary collision is descibed in DTUNUC by the fragmentation of two color-neutral parton–parton chains. In DPMJET, also multiple soft chains and multiple minijets are considered. Those chains are constructed from the valence quark systems or – in the case of repeated scatterings of single hadrons – from sea-$q\bar{q}$ pairs and sea-qq–$\bar{q}\bar{q}$ pairs of the interacting hadrons.

For nucleus–nucleus collisions the single particle densities in rapidity space, in the two-chain approximation, are given by

$$\begin{aligned}\frac{dN^{AB}}{dy} = \frac{1}{\sigma_{AB}} \sum \sigma_{n_A,n_B,n} \{ & \Theta(n_B - n_A)[n_A(N^{qq^A - q_v^B} + N^{q_v^A - qq^B}) \\ & + (n_B - n_A)((1-\alpha)(N^{q_s^A - qq^B} + N^{\bar{q}_s^A - q_v^B}) + \alpha(N^{(q\bar{q})_s^A - qq^B} + N^{(qq)_s^A - q_v^B})) \\ & + (n - n_B)((1-2\alpha)(N^{q_s^A - \bar{q}_s^B} + N^{\bar{q}_s^A - q_s^B}) \\ & + \alpha(N^{q_s^A - (qq)_s^B} + N^{(qq)_s^A - q_s^B}) + \alpha(N^{\bar{q}_s^A - (\bar{q}\bar{q})_s^B} + N^{(\bar{q}\bar{q})_s^A - \bar{q}_s^B}))] + (A \to B)\}. \end{aligned} \tag{9}$$

Here n denotes the total number of inelastic collisions between n_A and n_B participating nucleons from the projectile and target nuclei, and α is the rate of diquark pairs to q–$\bar{q}$ pairs in the proton sea. The rapidity densities, on the right-hand side, are represented by capital N; for instance, for diquark–quark chains: $N^{qq^A - q_s^B}$.

The hadronization of single chains is handled by the Monte Carlo codes BAMJET [18,19] and DECAY [20] (both the codes have been modified for a convenient application in DTUNUC), or by the Lund code JETSET-7.3 [21].

2.2.2. *The Cronin effect*

In nuclear collisions, the partons at the sea and valence chain ends carry transverse momenta from different sources:

(i) The intrinsic parton transverse momentum in the hadron;

(ii) a transverse (and longitudinal) momentum resulting from the Fermi motion of the nucleons inside the nucleon. These first two kinds of transverse momentum were implemented into DTUNUC from the beginning;

(iii) during the passage of the chain end partons through nuclear matter, they suffer nuclear multiple scattering which changes (usually increases) their transverse momenta.

The multiple scattering of partons is known since a long time to be responsible for the so called *Cronin effect* [22] of particle production at large transverse momentum on nuclear targets. A similar enhancement of particle production in hadron–nucleus and nucleus–nucleus collisions, as compared to hadron–hadron collisions, has been observed in many experiments already at rather modest $p_\perp$.

At large $p_\perp$ this effect can be studied calculating the parton scattering pertubatively. Our rather low $p_\perp$ sea chain ends might be considered as the low $p_\perp$ limit of perturbatively scattered partons. We apply to them, as well as to the hard scattered partons, multiple scattering taking into account their path length inside the nuclear matter. We adjust the parameters in such a way that the measured $p_\perp$ ratios at rising transverse momenta are approximately reproduced by the code DTUNUC.

2.2.3. *Production of strange particles*

Studies of strangeness production within this model were given in [14,16]. The DPM is an independent string model. Since the individual strings are universal building blocks of the model, the ratio of *produced* strange particles over non-strange ones will be approximately the same in all reactions. However, since some strings contain sea quarks at one or both ends, and since strange quarks are present in the proton sea, it is clear that, by increasing the number of those strings, the ratio of strange over non-strange particles will increase. This will be the case for instance, when increasing the centrality in a nucleus–nucleus collision. It is obvious,

that the numerical importance of the effect will depend on the assumed fraction of strange over non-strange quarks in the proton sea. The rather extreme case leading to a maximum increase of strangeness is to assume a SU(3) symmetric sea (equal numbers of u, d and s flavors). We express the amount of SU(3) symmetry of the sea chain ends by our parameter s^{sea} (introduced in [16]) defined as $)s^{sea} = \langle s_s \rangle / (\langle u_s \rangle + \langle d_s \rangle)$ where the $\langle q_s \rangle$ give the average numbers of sea quarks at the sea chain ends. All results from DPMJET-II given in this paper are obtained with $s^{sea} = 0.5$. This corresponds approximately to the fraction of strange sea-quarks found in deep inelastic structure functions.

The Monte Carlo event generators based on dual parton model, like DPMJET-II, also provide charm and heavier flavours production. This feature of DPMJET has not yet been checked against experimental data, but in this paper we shall present a few very preliminary results about prompt muon production in cosmic ray cascades. We plan to discuss this topic in more detail in a future publication.

2.2.4. *Diffractive events*

Single diffraction within the dual parton model was studied in detail and compared to experimental data in [15,23]. Single diffraction dissociation is represented by a triple-pomeron exchange (high mass single diffraction) and a low mass component (low mass single diffraction) [3].

Diffractive processes characterized by the excitation of an initial hadron to intermediate resonances (low mass diffractive interactions) are introduced via a two channel eikonal formalism.

3. The event generator DPMJET-II

DPMJET, version II [2] uses the dual parton model for nuclear collisions as implemented in DTUNUC-1.04 [16], but for each elementary nucleon–nucleon collision the full system of multiple soft chains and multiple minijets as implemented in DTUJET93 [4] is used.

3.1. *Hadron–hadron collisions with DPMJET-II*

DPMJET-II, using the multiple soft chains and multiple minijets from DTUJET93, is expected to show, as DTUJET93, the same rise with energy of average multiplicities, of the rapidity plateau and average transverse momenta.

In Table 1 we compare DPMJET-II at 200 GeV with measured multiplicities of the most important secondary hadrons. The data are from Ref. [24]. The agreement is excellent.

The relevance of an event generator like DPMJET-II based on the dual parton model for hadron production cross sections in the cosmic ray energy region can only be claimed if the model (i) agrees with the best

Table 1
Comparison of average multiplicities of produced hadrons in proton–proton collisions at 200 GeV. The experimental data are from Ref. [24].

Particle	DPMJET-II	Exp.	Particle	DPMJET-II	Exp.
n_{ch}	7.66	7.69 ± 0.06	π^0	3.38	3.34 ± 0.24
n_-	2.82	2.85 ± 0.03	K^+	0.28	0.28 ± 0.06
p	1.34	1.34 ± 0.15	K^-	0.19	0.18 ± 0.05
n	0.62	0.61 ± 0.30	K_S^0	0.22	0.17 ± 0.01
π^+	3.17	3.22 ± 0.12	$\bar{p}$	0.07	0.05 ± 0.02
π^-	2.56	2.62 ± 0.06			

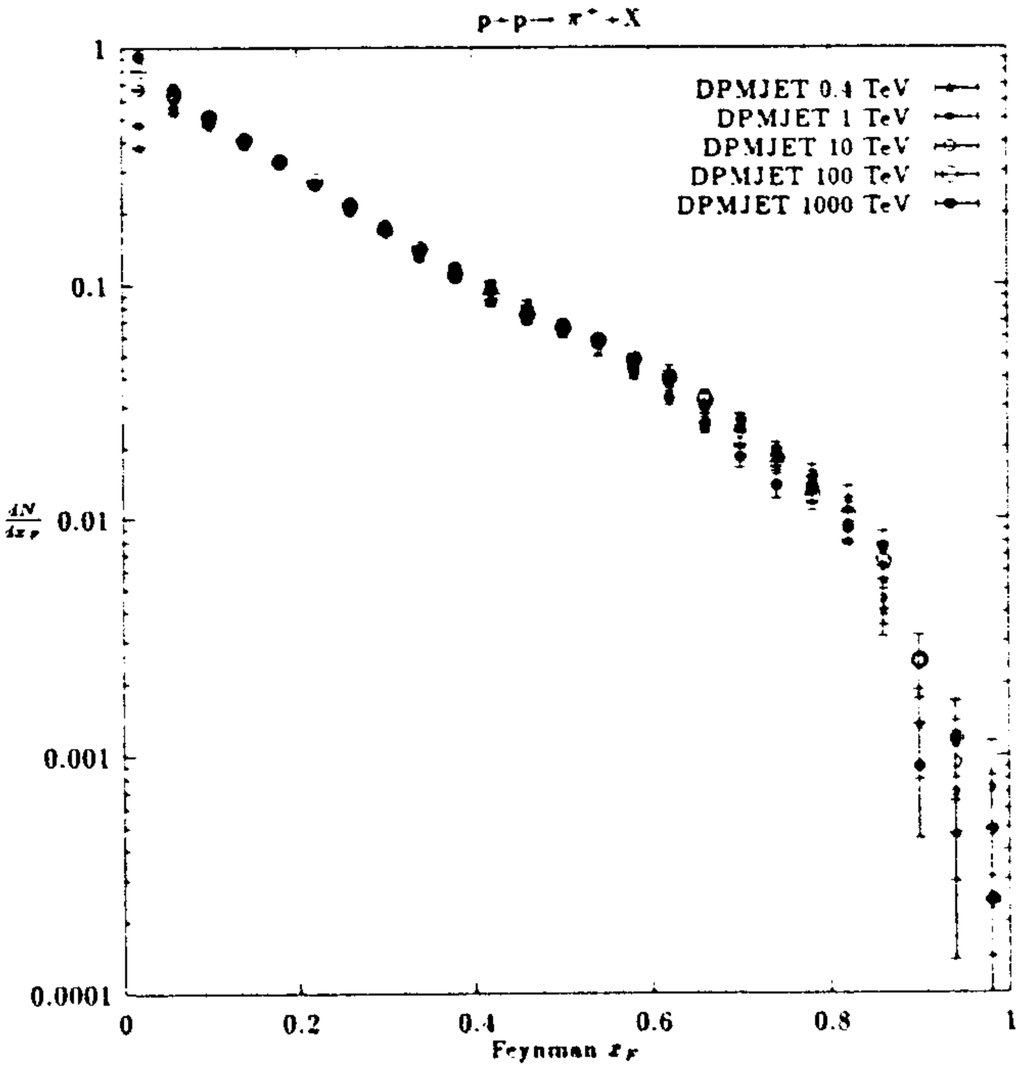

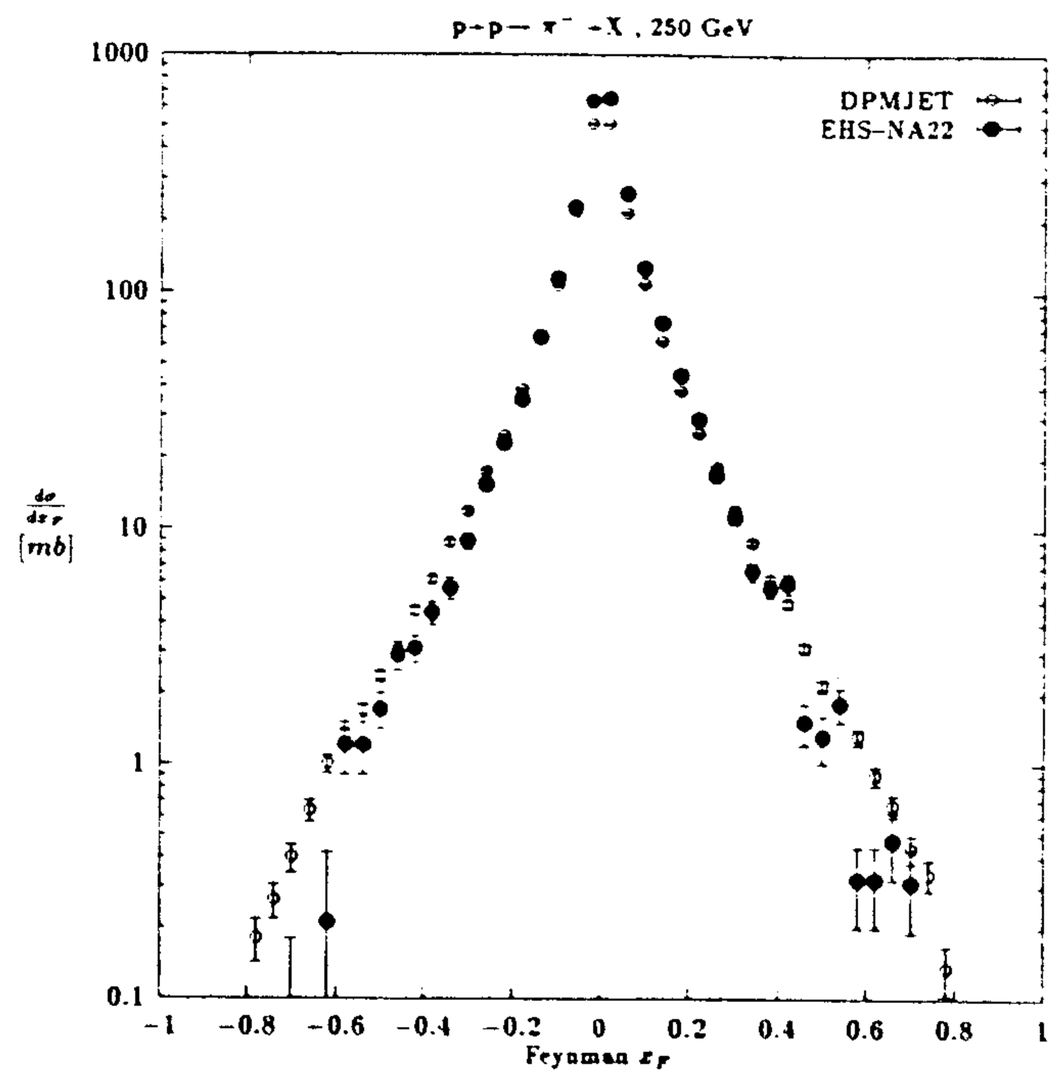

Fig. 1. Test of Feynman scaling in the production of π^+ in proton–proton collisions. The Feynman-x distributions were calculated with the dual parton model DPMJET-II. The energies shown in the plot are expressed in the lab-frame. The error bars shown in this plot, as in all other figures of this paper, are only statistical.

Fig. 2. Comparison of Feynman-x distributions of π^- mesons produced in proton-proton collisions at 250 GeV. The experimental data are from the EHS-NA22 Collaboration [25]. The calculation uses the dual parton model DPMJET-II.

available data in the accelerator energy range, and (ii) shows a smooth behaviour in the extrapolation to higher energies.

For the cosmic ray cascade in the atmosphere only hadron–nucleus (and nucleus–nucleus) collisions are relevant, with nitrogen (N) being the most important target nucleus. However, experimental data in the projectile fragmentation region are of much better quality in hadron–hadron, and especially proton–proton collisions than for collisions of hadrons with light nuclei. Therefore, we start with the study of proton–proton collisions.

In order to see whether data in the accelerator energy range with projectile energies well below 1 TeV are relevant at all, we study first the Feynman scaling behaviour of the model. In Fig. 1 we study the Feynman scaling of the produced secondary π^+ mesons. In most of the x_F region, say for $0.05 \leq x_F \leq 0.8$, we find Feynman scaling indeed very well satisfied in the dual parton model. The violations of Feynman scaling, which occur around $x_F = 0$ are connected with the well known rise of the rapidity plateau for all kinds of produced particles. For produced mesons, the statistics is not good enough to conclude whether Feynman scaling near $x_F = 1$ is strongly violated. However, in the Feynman x_F region $0.1 < x_F < 0.6$, scaling for the meson distributions is excellent, and this is important for the cosmic ray cascade development in the atmosphere (see the discussion in Section 6.3.5). We find also a strong violation of Feynman scaling for secondary nucleons around $x_F = 1$. This is connected with the diffractive component, which clearly violates Feynman scaling. This means, within the framework of the dual parton model, that experimental data in the fragmentation region (and the agreement of the model to them) are indeed very relevant also for the cosmic ray energy region.

In proton–proton collisions, we have the advantage that experimental data are available for Feynman x_F distributions $d\sigma/dx_F$ or $x_F d\sigma/dx_F$ integrated over transverse momentum. In hadron–nucleus collisions nearly all data are only double differential distributions. In the Monte Carlo calculation, we get much smaller error

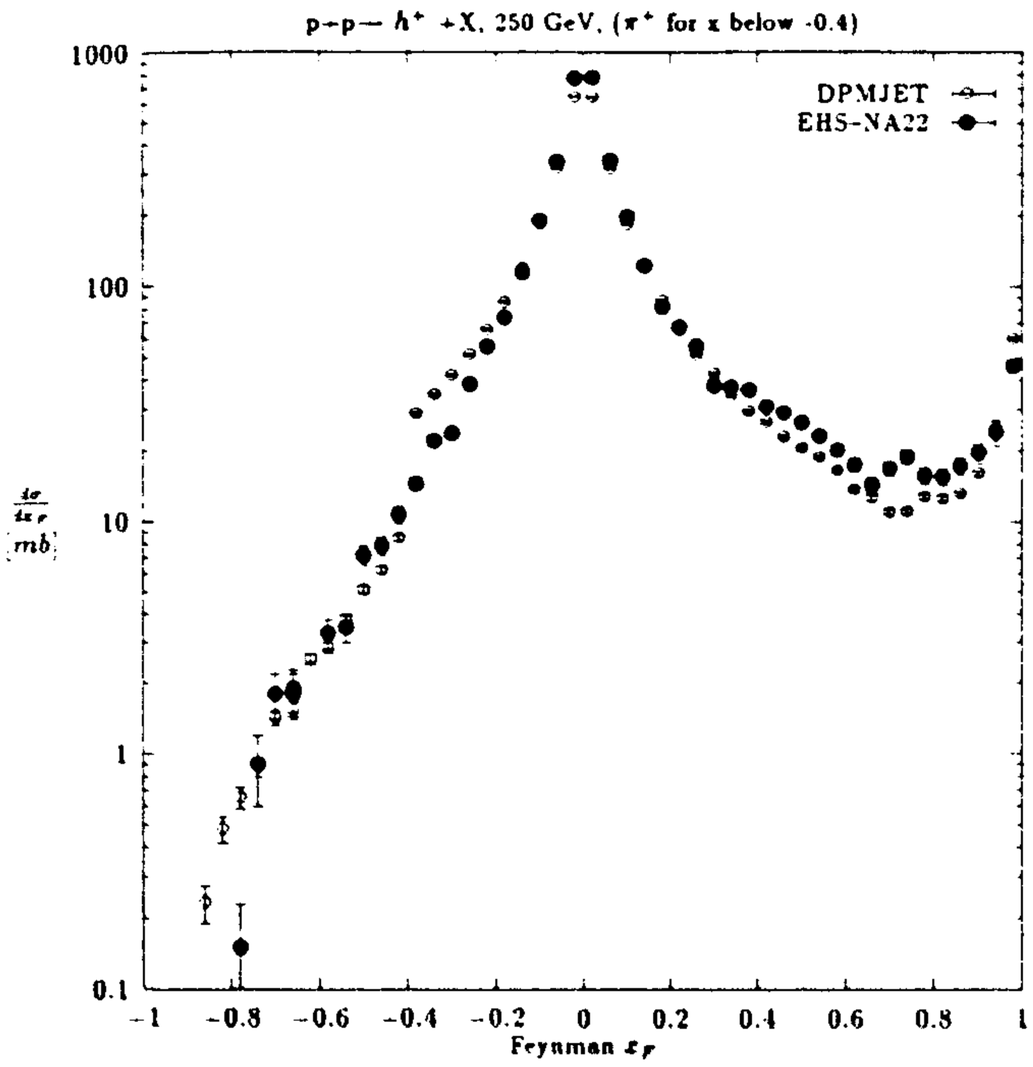

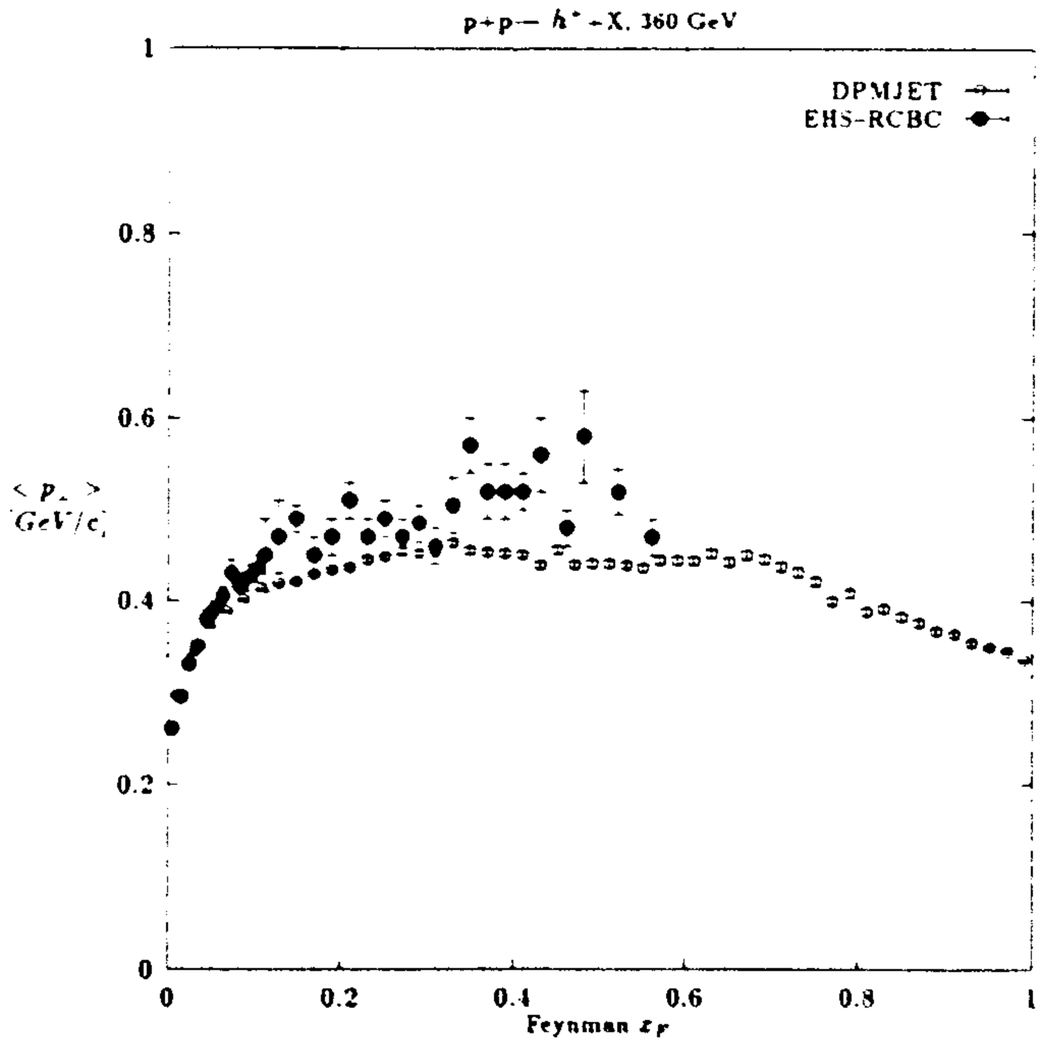

Fig. 3. Comparison of Feynman-x distributions of positively charged hadrons produced in proton–proton collisions at 250 GeV. The experimental data are from the EHS-NA22 Collaboration [25]. For $x_F \leq -0.4$ the experimental and calculated distributions refer to π^+ only. The calculation uses the dual parton model DPMJET-II.

Fig. 4. Comparison of the seagull effect in the reaction p+p→ h^+ +X at 360 GeV. The data are from the EHS-RCBC Collaboration [48]. The calculation uses the dual parton model DPMJET-II.

bars for single differential distributions than for double differential distributions. However, also in proton–proton collisions, the data are sometimes in contradiction.

Here we present only one comparison to experimental Feynman x_F distributions. The EHS-NA22 Collaboration [25] has data on $d\sigma/dx_F$ in 250 GeV proton–proton collisions. In Fig. 2 we compare the DPMJET results for π^- production in the forward and backward fragmentation regions and find a reasonable agreement. In Fig. 3 we compare with the production of positively charged hadrons for $x_F \geq -0.4$ and with π^+ production for $x_F \leq -0.4$; again the agreement is reasonable. In the projectile fragmentation region at large x_F this distribution is dominated by the leading protons from diffractive and nondiffractive events.

There seems to be an inconsistency between the multiplicities compared in Table 1 with data and the comparison of the x_F distributions near to $x_F = 0$ with data in Figs. 2, 3. In Table 1 we find a very good agreement between the average multiplicities, but in Figs. 2, 3 at $x_F = 0$ the model is below the data. The reasons for this different normalization is not clear. The model calculation includes in all cases diffractive events, this leads certainly to smaller central multiplicities than in nondiffractive events. However, in Fig. 3 we see the diffractive component also in the data. A different binning could give a different normalization at $x_F = 0$, but in Figs. 2 and 3 the binnings for the experimental data and for the model are identical.

In the fragmentation region the transverse momentum distributions and average transverse momenta are known to depend strongly on Feynman x_F. This effect is known under the name *seagull effect*. In Fig. 4 we compare DPMJET-II with data on the seagull effect measured by the EHS-RCBC Collaboration at 360 GeV and find a reasonable agreement. Unfortunately, experimental data on the seagull effect are usually limited to $x_F \leq 0.5$–0.6.

Table 2
Inelastic cross sections for proton–air and π^+–air collisions as calculated with DPMJET-II.

P_{lab} [TeV/c]	σ_{inel}^{p-air} [mb]	$\sigma_{inel}^{\pi^+-air}$ [mb]	P_{lab} [TeV/c]	σ_{inel}^{p-air} [mb]	$\sigma_{inel}^{\pi^+-air}$ [mb]
0.1	274.6	194.4	500	389.4	292.6
0.2	278.6	198.6	1000	399.6	301.0
0.5	286.2	208.8	2000	409.8	309.4
1	293.7	218.9	5000	423.3	320.6
2	302.5	228.7	10000	433.5	329.1
5	316.5	240.7	20000	443.6	337.5
10	333.1	247.8	50000	456.8	348.6
20	344.0	255.3	100000	466.7	357.0
50	355.8	265.6	200000	476.5	365.3
100	365.8	273.6	500000	489.4	376.1
200	375.9	281.7			

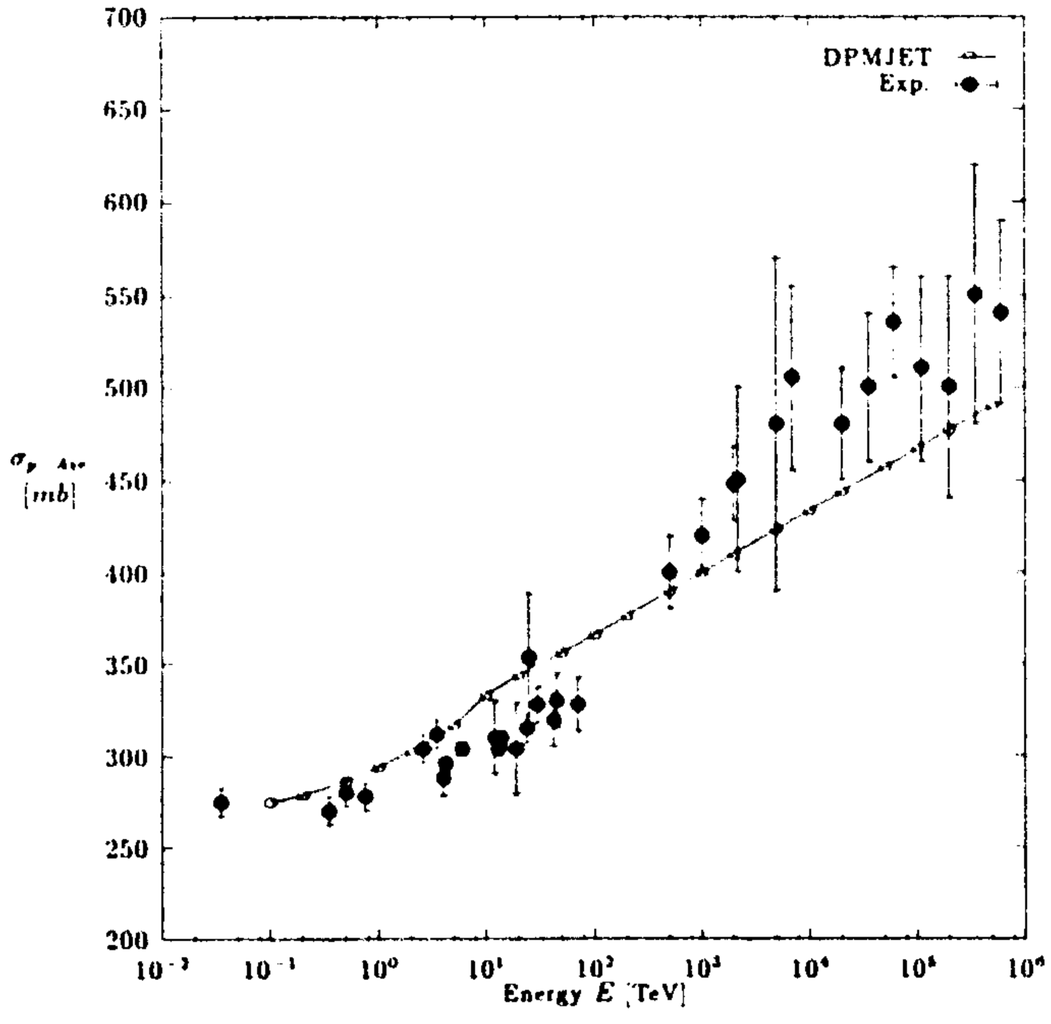

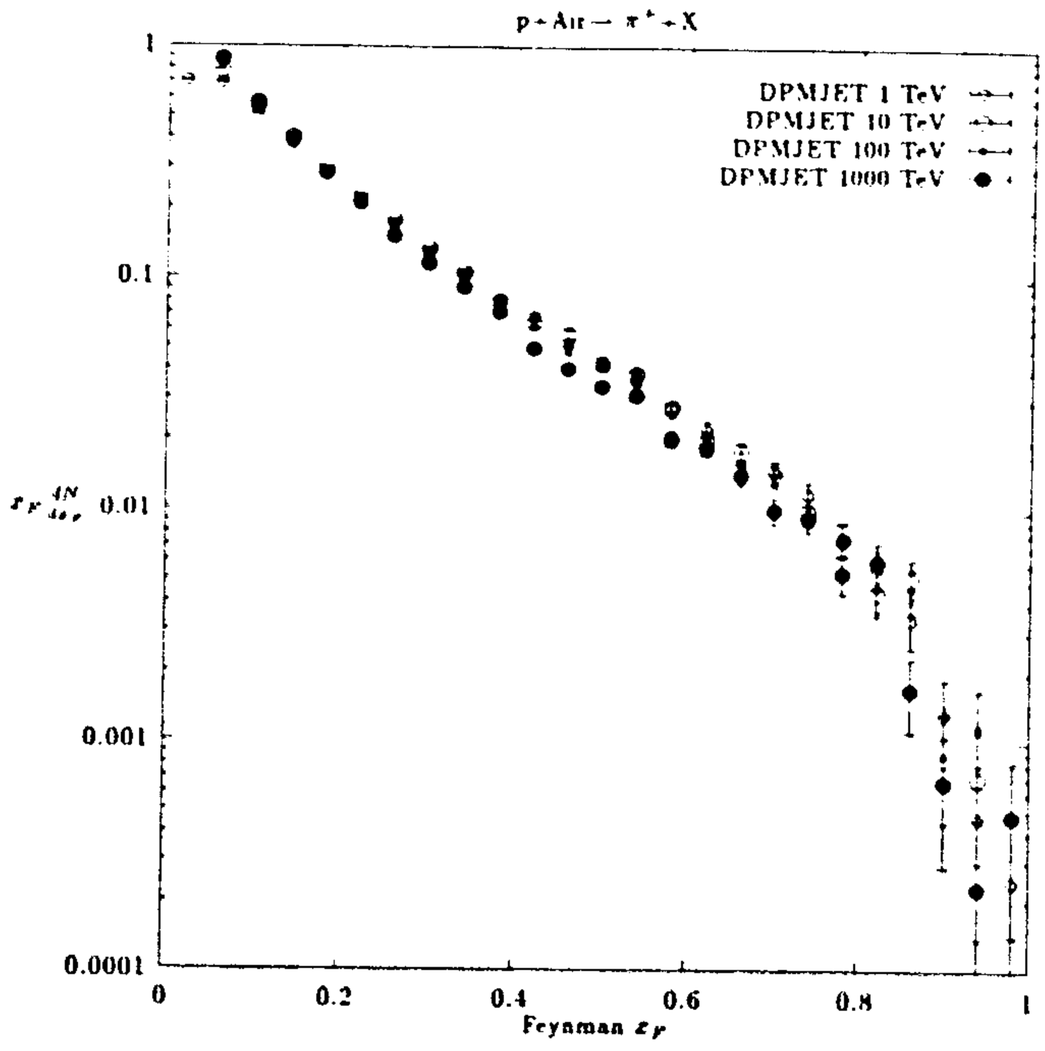

Fig. 5. The total cross section σ_{p-air} as function of the collision energy as calculated using the Glauber model in DPMJET-II. The calculation is compared to cosmic ray data collected by Mielke et al. [49]; a line is drawn to guide the eye.

Fig. 6. Test of Feynman scaling in the production of π^+ in proton–air collisions. The Feynman-x distributions were calculated with the dual parton model DPMJET-II.

3.2. Hadron–nucleus collisions with DPMJET-II

The Glauber model, which is part of DPMJET-II allows to calculate the inelastic hadron–nucleus cross sections. What we need for this calculation is the nuclear geometry and the elementary hadron–nucleus scattering amplitude.

In Table 2 we give for p–air and π–air collisions the inelastic cross sections calculated in this way by DPMJET-II. In Fig. 5 we compare the p–air cross sections with data from cosmic ray experiments.

In order to understand the relevance of accelerator data on particle production in hadron–nucleus collisions

for the cosmic ray cascade, we study again the Feynman scaling behaviour of p + air $\rightarrow \pi^+ + X$.

This is done in Fig. 6, where we plot the $x_F dN/dx_F$ distributions for laboratory energies of 1, 10, 100 and 1000 TeV. As in proton–proton collisions, we find again that Feynman scaling is very well satisfied in most of the x_F region. Exceptions are again the region around $x_F = 0$, where the rise of the rapidity plateau violates Feynman scaling and the region close to $x_F = 1$ for leading particles, where the diffractive component does not show Feynman scaling. Given this Feynman scaling behaviour, we can again conclude that accelerator data and their agreement to the model are indeed very relevant to the cosmic ray application of the model.

The change of hadron production with the mass of the nuclear target can be described by the function $\alpha(x_F)$, representing the cross section as

$$x_F \frac{d\sigma}{dx_F}^{p-A} = A^{\alpha(x_F)} x_F \frac{d\sigma}{dx_F}^{p-N} . \tag{10}$$

For the transition p–p to p–air this $A^{\alpha(x_F)}$ behaviour is not relevant, since we know that this kind of extrapolating h–A total cross sections to p–p does not give the correct p–p total cross section. Usually $\alpha(x_F)$ is determined using data for two or more different target nuclei without considering p–N collisions.

Unfortunately, there are no precise data (from the same experiment) where the differences of Feynman x_F distributions in p–p and p–light nucleus collisions could be checked. Therefore, for this transition, the best we can do at present is to rely on the model.

The results of double differential cross sections for inclusive hadron production in hadron–nucleus collisions have been represented in the form

$$E\frac{d^3\sigma}{d^3p}^{p-A} = A^{\alpha(x_F,p_\perp)} E\frac{d^3\sigma}{d^3p}^{p-N} . \tag{11}$$

With data on two different target nuclei, one can extract $\alpha(x_F, p_\perp)$ without the knowledge of $Ed^3\sigma/d^3p^{p-N}$. The data of Barton et al. [26] at 100 GeV and at a transverse momentum $p_\perp$ =0.3 GeV/c were used to get $\alpha(x_F)$ (in reality: $\alpha(x_F, p_\perp = 0.3\ \mathrm{GeV}/c)$). In the Monte Carlo calculation it is difficult to get such a good statistics at fixed $p_\perp$, to extract meaningfull $\alpha(x_F)$ values. This is just possible for single differential distributions in x_F. In Fig. 7 we compare the $\alpha(x_F)$ as obtained by Barton et al. [26] for pion production at $p_\perp = 0.3$ GeV/c with $\alpha(x_F)$ obtained from DPMJET-II results for all charged hadrons integrated over all $p_\perp$. The agreement in the x_F region of overlap is reasonable. For $x_F \rightarrow 0$ in the dual parton model we have the limit $\alpha(x_F \rightarrow 0) = 1$. This is actually also obtained from DPMJET-II. For large values of x_F the limiting $\alpha(x_F \rightarrow 1)$ from the data and from the Monte Carlo seems to be around 0.4.

The agreement with these $\alpha(x_F)$ data is the strongest point for the claim that the dual parton model, in the form of the DPMJET-II event generator, gives a good description of the nuclear dependence of hadron production in the fragmentation region. We stress however, once again, that these $\alpha(x_F)$ data are only for fixed $p_\perp$, and it would be highly desirable to obtain better data for the change of hadron production from proton–proton collisions to collisions of protons with light target nuclei.

In order to show the changes in the transverse momentum distributions from p–p to p–A collisions, one presents the data in the form of $p_\perp$ ratios

$$R(p_\perp) = \frac{Ed^3N/d^3p^{p-A}}{Ed^3N/d^3p^{p-p}} \tag{12}$$

or one uses the $\alpha(p_\perp)$ representation

$$E\frac{d^3\sigma}{d^3p}^{p-A} = A^{\alpha(p_\perp)} E\frac{d^3\sigma}{d^3p}^{p-N} . \tag{13}$$

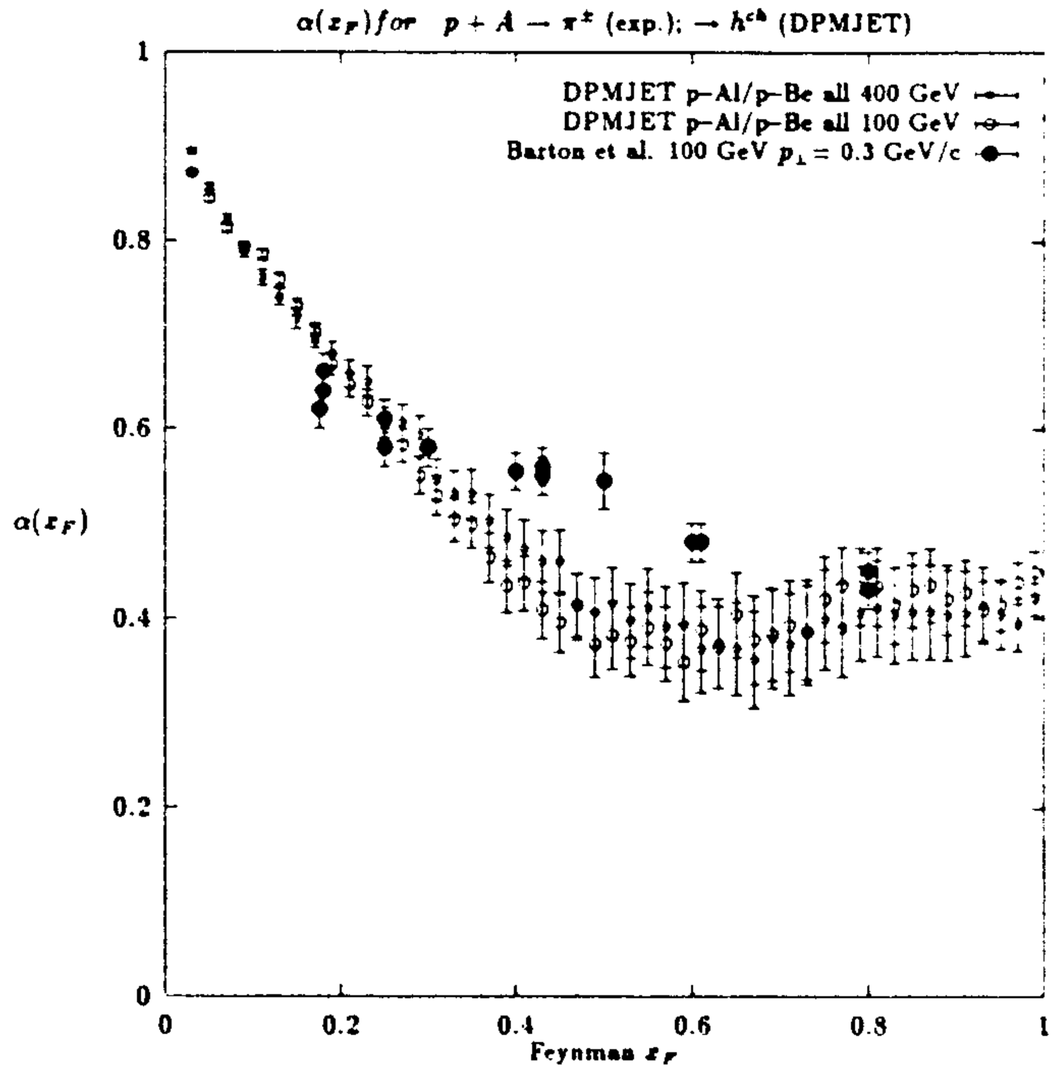

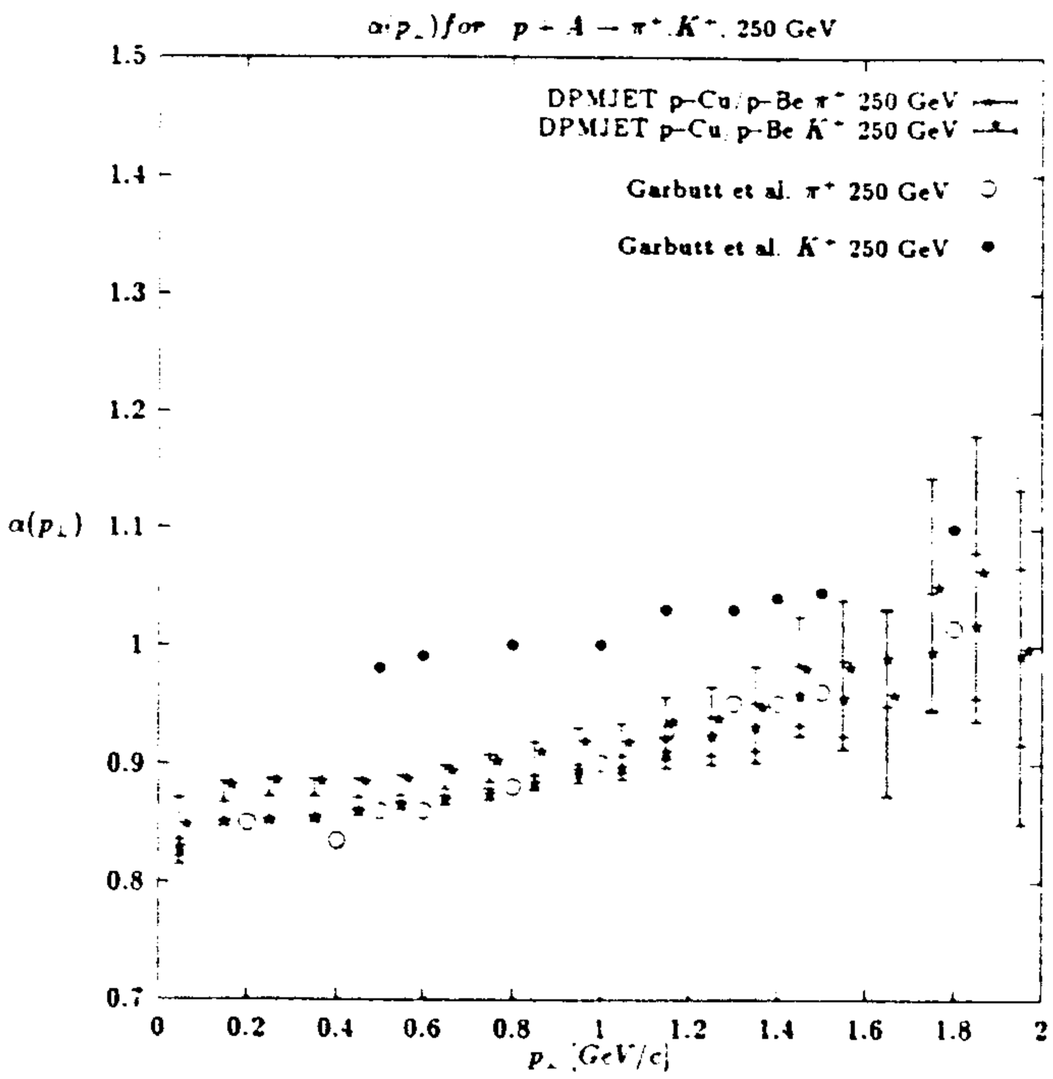

Fig. 7. The nuclear dependence of the Feynman-x distribution in hadron–nucleus collisions is represented in the form $d\sigma/dx_F^{h-A} = A^{\alpha(x_F)} d\sigma/dx_F^{h-p}$. We compare $\alpha(x_F)$ as determined by Barton et al. [26] for pion production at $p_\perp = 0.3$ GeV/c with the DPMJET-II results for all charged hadrons at all values of $p_\perp$.

Fig. 8. The nuclear dependence ot the $p_\perp$ distributions in proton–nucleus collisions is represented in the $A^{\alpha(p_\perp)}$ form. We compare data from Garbutt et al. [27] for produced π^+ and K^+ with the results of the dual parton model DPMJET-II. All data are at 250 GeV laboratory energy.

In Fig. 8 we compare DPMJET-II with $\alpha(p_\perp)$ data from Garbutt et al. [27]. The data and the calculations are only for π^+ and K^+. We find a rather good agreement with the data for π^+. For K^+ DPMJET-II gives systematically $\alpha(p_\perp)$ values larger than for π^+, but below the data from the experiment.

In Fig. 9 we present how the seagull effect as calculated in DPMJET-II for p–air collisions scales with energy. The calculations are at energies between 1 TeV and 1000 TeV . At all energies $\langle p_\perp(x_F)\rangle$ rises significantly with x_F (at least in the region $x_F \leq 0.5$). At the same time the average transverse momentum rises at all x_F values strongly with the collision energy. This rise in the model is mainly due to the rise of minijet production and due to the Cronin effect in the nuclear target.

3.3. Nucleus–nucleus collisions

The same Glauber model which gives the hadron–air inelastic cross sections is also able to calculate nucleus–nucleus inelastic cross sections. In Fig. 10 we present nucleus–air inelastic cross sections as calculated with DPMJET-II in the energy range 0.1 TeV to 10^7 TeV. All these cross sections rise with the energy, but the relative rise of the cross sections from the lowest to the highest energy is smaller for heavy projectiles, since at small impact parameters the nuclei become black already at lower energies.

Instead of the proper sampling of nucleus–nucleus scattering events, an approximation often applied is the so called superposition model. There are two different possible superposition models:

(i) A nucleus–nucleus collision A–B with N_p participating projectile nucleons is approximated as the superposition of n_p simultaneous nucleon–nucleon collisions.

(ii) A nucleus–nucleus collision A–B with N_p participating projectile nucleons is approximated as the superposition of n_p simultaneous nucleon–B collisions.

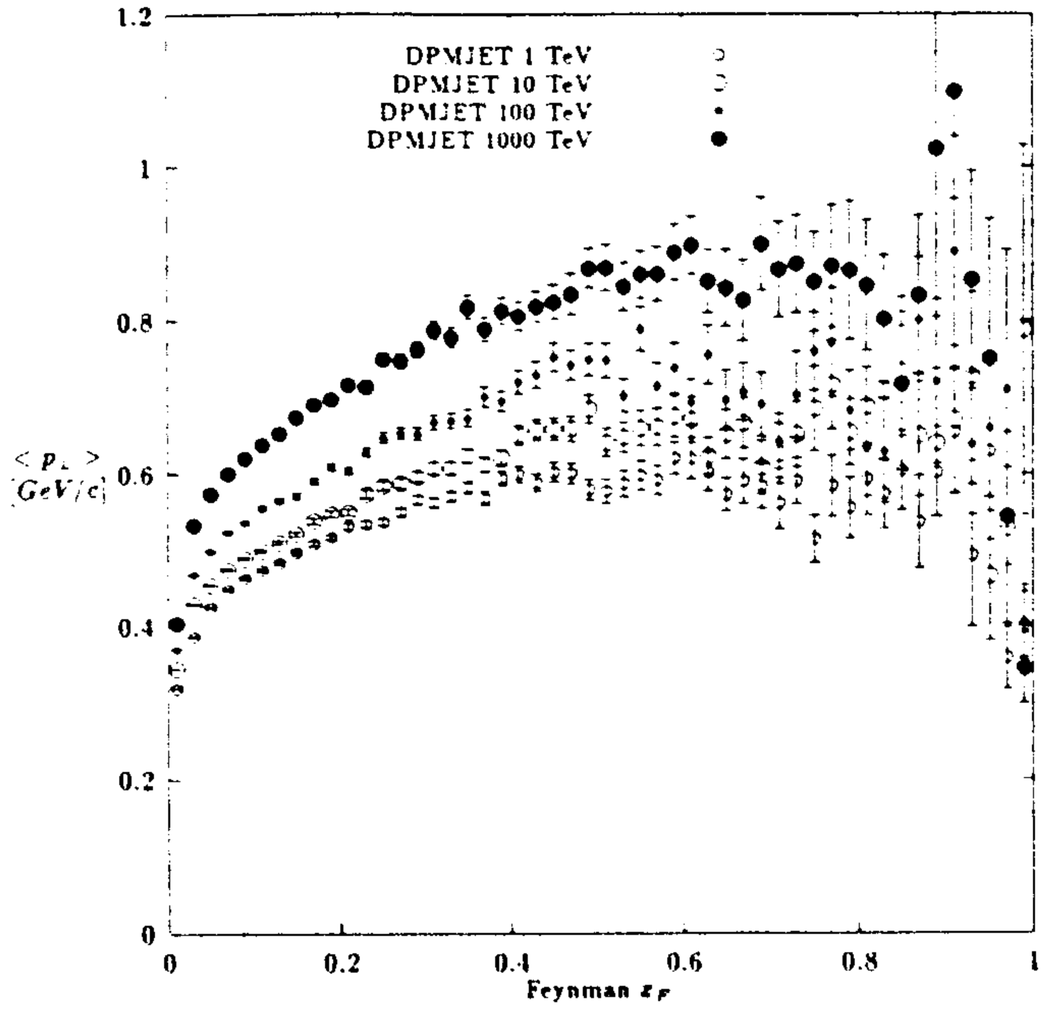

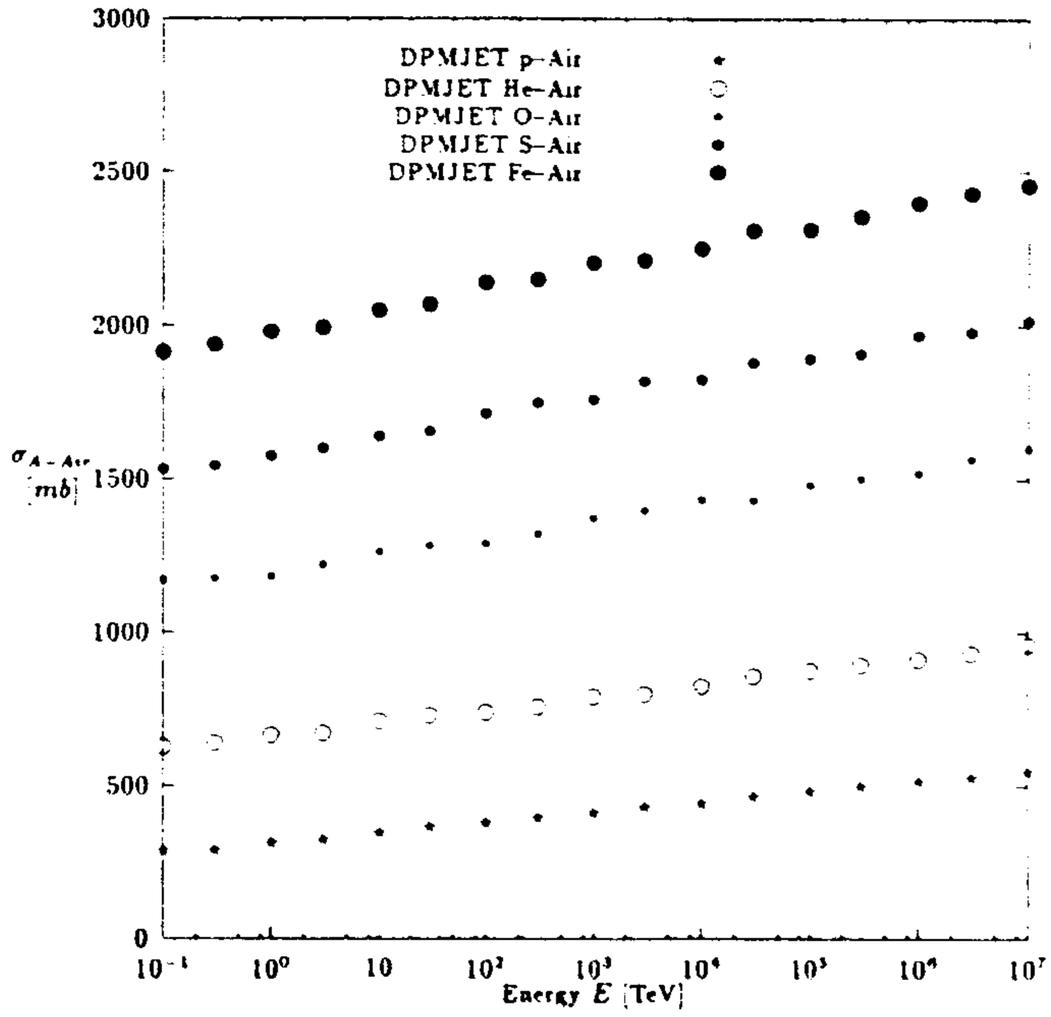

Fig. 9. The seagull effect as calculated from DPMJET-II for proton–air collisions at laboratory energies between 1 and 1000 TeV.

Fig. 10. Total nucleus–air cross sections $\sigma_{A-\mathrm{air}}$ as a function of the collision energy as calculated using the Glauber model in DPMJET-II.

Table 3
Comparison of average multiplicities $n_{\pi^\pm}^{\mathrm{C-air}}$ calculated in C–air collisions at different energies with the expectations in two different superposition models. N_p is the average number of projectile nucleons taking part in the inelastic C–air collision. The energies given are the energies per nucleon in the laboratory frame.

Energy [TeV]	N_p	$n_{\pi^\pm}^{\mathrm{C-air}}$	$n_{\pi^\pm}^{p-p}$	$n_{\pi^\pm}^{p-\mathrm{air}}$	$N_p n_{\pi^\pm}^{p-p}$	$N_p n_{\pi^\pm}^{p-\mathrm{air}}$
10	4.21	27.96	4.35	6.76	18.31	28.46
100	4.45	46.89	6.56	11.35	29.19	50.51
1000	4.69	73.71	9.31	17.45	43.66	81.84

In Table 3 we present the calculated particle multiplicities. It is also important to investigate the behaviour of the "spectrum weighted moments", defined as:

$$Z_i^{A-B} = \int_0^1 x_L^{1.70} \frac{dN^{A+B\to i+X}}{dx_L} dx_L \tag{14}$$

where $i = \pi, K, \ldots$ and $x_L = E_i/E_A$ in the target B rest frame; x_L is a good approximation of x_F in the projectile fragmentation region. The exponent 1.70 is approximatively the integral spectral index of the primary cosmic ray energy spectrum. The inclusive production of secondary particles of type i in cosmic ray cascades has been shown to depend upon the relevant Z functions [28]. These values, as calculated using DPMJET-II for C–air collisions, are given in Table 4. The comparisons in Tables 3 and 4, with both versions of the superposition model show that the superposition is only a very rough and unreliable approximation to real nucleus–nucleus collisions. So far DPMJET-II has not been checked against particle production in heavy ion experiments. We plan to make these comparisons.

Table 4
Comparison of $Z_{\pi^\pm}$-moments calculated in C–air $\rightarrow \pi^\pm + X$ at different energies with the expectations in two different superposition models. N_p is the average number of projectile nucleons taking part in the inelastic C–air collision. The energies given are the energies per nucleon in the laboratory frame.

Energy [TeV]	N_p	Z_π^{C-air}	Z_π^{p-p}	Z_π^{p-air}	$N_p Z_\pi^{p-p}$	$N_p Z_\pi^{p-air}$
10	4.21	0.3619	0.076	0.067	0.3200	0.2821
100	4.45	0.3778	0.076	0.069	0.3382	0.3071
1000	4.69	0.3872	0.076	0.068	0.3564	0.3189

4. DPMJET-II at cosmic ray energies

4.1. Important differences between the two-component dual parton model and minijet models

There is no scientific reason, not to call the two-component dual parton model (the two components are the soft pomeron and the hard pomeron or the minijets) also a minijet model. Minijet models too have a soft and a hard component. The reason not to use the term minijet model for DPMJET is connected with the fact that the name minijet model so far was only used for models which use a critical pomeron with an intercept $\alpha(0) = 1$. In such a minijet scheme it is then claimed that all the rise of the cross sections with energy is due to the rise of the minijet cross sections. This is not so in our model, therefore we avoid to use the name minijet model.

The supercritical pomeron was used in the two-component DPM from the beginning [5], while the so called minijet models use the critical pomeron with $\alpha(0) = 1$ from Durand and Pi [29] over Gaisser and Halzen [30], SIBYLL [31] up to HIJING [32].

There are important differences which result from this different approach:

(i) Both kinds of models determine the free parameters of their model in a fit to total, inelastic and elastic cross sections. Both models obtain acceptable fits, we have reported even about the fits using a critical pomeron elsewhere [7], but, of course, if at the end of the fit we treat the pomeron intercept $\alpha(0)$ as a free parameter instead to fix it to $\alpha(0) = 1$, the fit improves. In all situations (fits using different parton structure functions to calculate the minijet cross sections) we obtain the intercept larger than one, namely $\alpha(0) \approx 1.07$. These better fits to the data are our main argument for the continuing presence and even rise of soft hadron production at the highest energies.

(ii) Due to these different starting points, the chain structure of the models differ: in both models we have a pair of soft valence–valence chains (resulting from cutting one soft pomeron) and in both models we have minijets. Only in the two component dual parton model we have in addition soft sea–sea chains with soft sea quarks at their ends. The number of these chains increases with energy and a substantial part of the rise of the multiplicity and rapidity plateau results from this mechanism.

(iii) The x-distributions of soft sea quarks are determined by the Regge behaviour, and behave like $1/\sqrt{x}$ for sea as well as valence quarks. The minijets are calculated from the deep inelastic structure functions with (depending on the parametrization for the structure functions used) a behaviour like $1/x$ or $1/x^{1.5}$. In the dual parton model the Feynman x_F distributions resulting from fragmenting valence chain ends (which dominate at small energy) and from fragmenting soft sea chain ends do not differ; this is the source of the excellent Feynman scaling and the nearly energy independent spectrum weighted moments. In the minijet models all chains, except the single valence chain pair which dominates at low energy, are minijets with the much softer x-distribution. Therefore in these models Feynman scaling is more strongly violated and the spectrum weighted moments decrease with the collision energy. The rise of the minijet component in the dual parton model leads of course to the same effect, this effect is however smaller, since not all of the rise of particle production is due to the minijets.

There are further differences in these models, which result from the parton structure functions used to calculate

Table 5
$Z_{\pi\pm}$ and $Z_{K\pm}$ moments and leading baryon elasticities K_{ln} in p–p and p–air collisions.

Collision energy [TeV]	p–p Z_π	p–p Z_K	p–p K_{ln}	p–air Z_π	p–air Z_K	p–air K_{ln}
0.2	0.077	0.0094	0.45			
0.4	0.076	0.0092	0.45			
1	0.076	0.0093	0.45	0.067	0.0098	0.37
10	0.076	0.0092	0.44	0.069	0.0099	0.33
100	0.076	0.0095	0.42	0.068	0.0102	0.31
1000	0.075	0.0093	0.40	0.066	0.0101	0.27

Table 6
$Z_{\pi\pm}$ and $Z_{K\pm}$ moments in π^+–p and π^+–air collisions.

Collision energy [TeV]	π^+–p Z_π	π^+–p Z_K	π^+–air Z_π	π^+–air Z_K
0.2	0.26	0.019	0.24	0.018
1	0.27	0.018	0.23	0.017
10	0.27	0.018	0.23	0.016
100	0.26	0.018	0.21	0.016
1000			0.19	0.015

Table 7
$Z_{\pi\pm}$ and $Z_{K\pm}$ moments in K^+–p and K^+–air collisions.

Collision energy [TeV]	K^+–p Z_π	K^+–p Z_K	K^+–air Z_π	K^+–air Z_K
0.2	0.093	0.171	0.082	0.156
1	0.092	0.181	0.084	0.156
10	0.091	0.188	0.082	0.145
100	0.086	0.183	0.080	0.132
1000			0.076	0.113

the minijet production cross sections. In DPMJET-II like in DTUJET93 we use the MRS[D–] [33] structure functions with a $1/x^{1.5}$ singularity. The first HERA data seem to favor just these singular parton distribution functions [34]. Using these structure functions, instead of the ones with $1/x$ singularity, the average transverse momenta rise more strongly with energy.

4.2. *Spectrum weighted moments*

In Table 5 we present spectrum weighted moments Z_π and Z_K according to DPMJET-II in p–p and p–air collisions and elasticities for the leading baryon K_{ln} (K_{ln} is defined as the average energy fraction carried by the single most energetic baryon in each event). We find, as explained already in the last Section, Z_π and Z_K moments rather constant as function of the collision energy. The moments for p–air collisions are smaller than for p–p collisions. This decrease is connected with the $\alpha(x_F)$ behaviour as given in Fig. 7. The elasticities K_{ln} decrease with energy. This decrease will be discussed in the next section.

In Tables 6 and 7 we give Z_π and Z_K moments in π^+–p, π^+–air, K^+–p and K^+–air collisions. Again, the

Table 8
Comparison of $Z_{\pi^\pm}$ and $Z_{K^\pm}$ moments in p–air collisions between DPMJET-II, HEMAS [35] (the present numbers result from a recent version of this code) and SIBYLL [31].

Energy [TeV]	DPMJET Z_π	HEMAS Z_π	SIBYLL Z_π	DPMJET Z_K	HEMAS Z_K	SIBYLL Z_K
1	0.067	0.061	0.072	0.0098	0.0104	0.0073
10	0.069	0.057	0.068	0.0099	0.0113	0.0071
100	0.068	0.056	0.067	0.0102	0.0116	0.0070
1000	0.066	0.056	0.066	0.0101	0.0123	0.0070

Table 9
Average energy fractions K_h in p–air collisions as calculated with DPMJET-II. Please note that all the K_h do not add up to 1.0, since most hyperons and antihyperons as well as antineutrinos are not included in the table.

Energy [TeV]	K_p	$K_{\bar{p}}$	K_n	K_{π^+}	K_{π^-}	K_{K^+}	K_{K^-}	K_Λ	K_{π^0}	$K_{K^0_S+K^0_L}$
1	0.265	0.011	0.093	0.167	0.138	0.024	0.018	0.023	0.174	0.041
10	0.233	0.012	0.091	0.175	0.147	0.025	0.020	0.022	0.181	0.044
100	0.212	0.013	0.088	0.179	0.154	0.026	0.022	0.022	0.185	0.046
1000	0.189	0.014	0.083	0.185	0.162	0.027	0.023	0.021	0.191	0.049
10000	0.168	0.015	0.077	0.190	0.169	0.029	0.025	0.020	0.198	0.052
100000	0.152	0.016	0.075	0.194	0.173	0.029	0.026	0.020	0.201	0.054

moments for the produced particles are rather constant with rising energy, while the moments for the leading hadrons decrease systematically with rising energy.

In Table 8 we compare the Z_π and Z_K moments calculated with DPMJET-II in p–air collisions with the ones resulting from HEMAS [35] and SIBYLL [31]. The agreement of the moments, especially those for charged pions from DPMJET-II and from SIBYLL, is certainly much better than what expected from the errors of the experimental data used to tune the parameters of the models. As far as the Z_K moments are concerned, DPMJET and HEMAS provide similar results, while SIBYLL is about 30% lower.

4.3. Average energy fractions

In Table 5 we presented already the elasticities K_{ln} for leading baryons as calculated from DPMJET-II for p–p and p–air collisions. In Table 9 we present the average energy fractions K_h carried by secondary hadrons of kind h in p–air collisions as calculated from DPMJET-II for the most important secondaries as function of the energy.

We observe in Tables 5 and 9 a decrease with energy of the average energy fractions of all leading baryons (p, n and Λ), while the average energy fractions of all newly produced kinds of hadrons increase with energy. A large part of this effect is due to the diffractive component.

In the two-component dual parton model [4] we obtain inelastic cross sections rising with energy like $\log^2 s$. The single diffractive cross sections, where the experimental data are not really a guidance, seem in the model at high energy to approach an energy independent value. A similar result was obtained recently by Gotsman, Levin and Maor [36]. The double diffractive cross sections in the model behave similarly.

The leading hadron average energy fractions are particularly large in diffractive events. If the relative fraction of diffractive events decreases with rising energy, we expect a decrease of the average energy fraction of the leading hadrons and a corresponding increase of the average energy fraction of produced hadrons as found in Table 9. In this situation, we stress the importance of experimental measurements of the hadron production

in the fragmentation region, including the measurement of diffractive cross sections at the highest available accelerator energies at the Fermilab Collider. Without such experimental data, we have only the models to extrapolate into the cosmic ray energy region.

4.4. Upper energy limit for DPMJET-II calculations

Presently DPMJET-II is able to run up to energies of approximately 10^{18} eV in the lab system. There are trivial reasons for this limit (dimensions in fields to be defined during initialization), which could result in a failure when running at higher energies. Such problems would be easy to solve, but, besides these trivial reasons, there are physical reasons which prevent the use of the code at higher energies.

The most important of these reasons is connected with the minijet component. The way in which the minijet component is implemented in DTUJET93 and DPMJET-II is described in Ref. [4]. This method is expected to break down for structure functions with $1/x^{1.5}$ singularities (for sea quarks and gluons) at higher energies. These structure functions are suggested by the first measurements at the HERA accelerator. For the older structure functions with a $1/x$ singularities, it would be rather straightforward to define the minijet component at higher energies, but this might not correspond to the correct physics. We have certainly ideas on the way to extend the treatment of the minijet component up to higher energies, but this would be connected with large modifications in the model, which need a relevant amount of time.

5. The shower Monte Carlo HEMAS-DPM

We have interfaced the interaction model described in this paper with the shower code contained in the HEMAS code [35]. HEMAS is a Monte Carlo for the calculation of the hadronic, electromagnetic and muonic components in air showers. The first version of the code (HEMAS-1) has been described in detail in Ref. [35]. It was able to follow in three dimensions the shower development in the standard atmosphere, and contained also a code for muon propagation in standard rock. The original interaction model was derived by a multi-cluster parametrization of minimum bias events as detected at hadron colliders, together with the inclusion of nuclear target effects. Since its publication and release, this code has been extensively used, in particular inside the MACRO Collaboration [37–41], and different improvements have been implemented in it. In particular it has been interfaced to a new code for the nuclear fragmentation [42] ("semi-superposition model", see Section 5.2), and to a new code for the propagation of muons in the rock [43] (see Section 5.5). Furthermore, new routines for the calculation of the electromagentic shower size have been implemented (see Section 5.4).

In the following we shall describe the implementation of the hadronic event generator DPMJET-II inside the shower code, which from now on will be referred as HEMAS-DPM.

5.1. Secondary particles followed in HEMAS-DPM

The original list of particles followed in the shower (γ, $e^{\pm}$, π^0, $\pi^{\pm}$, $K^{\pm}$, K^0, $\bar{K}^0$, p, n, $\mu^{\pm}$, ν_μ, $\bar{\nu}_\mu$, ν_e, $\bar{\nu}_e$) has been enlarged to include antinucleons ($\bar{p}$, $\bar{n}$) and lambdas (Λ^0, $\bar{\Lambda}^0$) – not produced in the original HEMAS interaction model – and moreover to include a list of nuclei ${}^{4}_{2}$He, ${}^{9}_{4}$Be, ${}^{12}_{6}$C, ${}^{14}_{7}$N, ${}^{16}_{8}$O, ${}^{20}_{10}$Ne, ${}^{24}_{12}$Mg, ${}^{28}_{14}$Si, ${}^{32}_{16}$S, ${}^{40}_{18}$Ar, ${}^{48}_{22}$Ti, ${}^{52}_{24}$Cr, ${}^{56}_{26}$Fe. These nuclei can be primary cosmic rays and/or fragments of previous nucleus–air interactions. In the original HEMAS code the superposition scheme was adopted: a shower generated by a primary of mass $A > 1$ and energy E_0 is simulated as A showers induced by nucleons of energy E_0/A, interacting independently since the top of the atmosphere.

From now on we will refer to four categories of particles in the shower: the electromagnetic particles (γ, $e^{\pm}$), the hadrons (π^0, $\pi^{\pm}$, $K^{\pm}$, K^0, $\bar{K}^0$, p, n, $\bar{p}$, $\bar{n}$, Λ^0, $\bar{\Lambda}^0$), the neutrinos (not discussed in this paper) and the nuclei (He, Be, C,..., Fe).

The presence of nuclear projectiles, distinct from nucleons, demands a brief discussion of the possible options for their treatment. In the following we give some detail about the the features of the HEMAS-DPM code.

5.2. *The nuclear fragmentation*

If the primary cosmic ray is a nucleus with mass $A > 1$, the shower can be generated in three different ways:

(i) Through the superposition of A independent nucleon showers: each shower starts at a depth calculated according to the proton–air cross section. From now on, this very simplified, but quite unrealistic, model will be referred as "pure superposition" model (ps).

(ii) Through the so-called semi-superposition model (ss): here also the shower is the result of A independent nucleon showers, but the start depth of each shower is determined by calculating the successive fragmentation depths, starting from the initial nucleus A down to the A free nucleons. Thus, the cross sections of nuclei with mass $\leq A$ (all possible fragments) are required in this model, together with a scheme for the nuclear fragmentation and for the determination of the fraction of wounded nucleons (nucleons of the projectile which directly interact inside the target nucleus). In the code HEMAS-1 a model for nuclear fragmentation was included which is now obsolete. A new semi-superposition model NUCLIB [42] has now been included inside HEMAS-DPM.

(iii) Through a direct nucleus-air interaction (di). This option is available only when using the DPMJET-II hadronic interaction code (see Section 3.3). Thus it is a feature of HEMAS-DPM, not available in HEMAS-1.

5.3. *The hadron (nucleus)–air interaction*

The hadron (nucleus)–air interaction is generated choosing one of two different models, together with the different options concerning nuclear fragmentation described above. In total, the shower can be simulated using five different possible configurations:

(i) Pure superposition + the HEMAS original hadron–air model (HEMps);
(ii) semi-superposition + the HEMAS original hadron-air model (HEMss);
(iii) pure superposition + the DPMJET-II model (DPMps);
(iv) semi-superposition + the DPMJET-II model (DPMss);
(v) direct nucleus–air interaction with the DPMJET-II model (DPMdi).

Clearly, the distinction among "ps", "ss" and "di" is relevant only for primaries with mass $A > 1$. In this paper the calculations are performed in the configurations HEMps, DPMps and DPMdi and the results compared (see Section 6).

5.3.1. *The original HEMAS model*

The HEMAS-DPM code contains minor modifications respect to the HEMAS-1 version for what concern the hadron–air interaction. Like in HEMAS-1, here also the only possible projectiles are π, K and nucleons; neither antinucleons nor lambdas and antilambdas, nor nuclei are admitted.

The only relevant change respect to HEMAS-1 is the K/π ratio in hadron–air interactions. In HEMAS-1 this ratio was assumed 1.45 times the value for an hydrogen target. Even though experimental data confirm the enhancement of the strangeness production when increasing the target mass (see Fig. 8), a so large correction factor is not justified. We assume here a factor 1.1, since we obtain, in the average, such a factor from test runs with DPMJET.

5.3.2. *The DPMJET-II model*

This code has been described in detail in Section 3. Here we only remind that, inside the shower code HEMAS-DPM:

- the possible projectiles are all the hadrons and nuclei listed above;
- the final particles of the interaction can be hadrons, nuclei, prompt muons and prompt neutrinos (the charmed mesons decay promptly inside the interaction section).

Here it is worthwhile spending a few words about the way in which the production of secondary nuclei is implemented in the model. DPMJET gives all the non-wounded nucleons of both projectile and target, plus the excitation energy. At present, DPMJET calculates the excitation energy only for the rest nucleus resulting from the target. In principle one should use the excitation energy to simulate the evaporation and de-excitation. We plan to implement such an algorithm in the same way as it is already contained in the FLUKA shower code [44]. An effort will be also dedicated to the problem of calculating the excitation energy for the projectile rest nucleus. The last stage of nuclear fragmentation which might follow for highly excited rest-nuclei is rather unclear at present; a scheme following the one presented in Ref. [45] might be adapted. However, for the moment, we limit ourselves to a rather simple implementation of evaporation process, which always leads to one of the nuclei treated by HEMAS listed above. Although this is still preliminary, we emphasize that this is already a good approximation for the projectile nuclei which are considered here.

5.4. Calculation of the electromagnetic shower size

When an electromagnetic particle is produced in the shower it is not followed anymore; we only calculate the average number of electromagnetic particles that it would produce in its sub-shower at a given height above sea level (we took $h = 2000$ m a.s.l.). Similarly, when a hadron produced in the shower has an energy lower than a given threshold (we used $E_{thr} = 1$ TeV), we do not determine if it decays or interacts, but we again calculate the electromagnetic size at height h, associated to its sub-shower. The sum of all the sub-shower sizes provides the total shower size.

The formulae used for the size calculation depend only on the kind of particle (electromagnetic or hadronic), on the particle energy and on the slant depth of atmosphere between the particle production point and the atmospheric sampling level h. In HEMAS-DPM the formulae adopted are different respect to the first version HEMAS-1. Here in fact we make use of the parametrization of the results obtained using specialized e.m. codes (GEANT [46] and FLUKA [44]), for electrons, photons, and pions. For this purpose we have followed the scheme described in Ref. [47], with some further simplification. In particular we do not introduce the intrinsic fluctuations on the single sub-showers, since the fluctuations of the whole hadronic shower are found to dominate.

5.5. Muon propagation through the rock

Two codes are available in HEMAS-DPM for the simulation of the muon transport through the rock:

(i) The original HEMAS code. No modifications have been made on the code, described in Ref.[35] (and references therein).

(ii) The Lipari and Stanev code. This code has been developed by P. Lipari and T. Stanev and is described in detail in Ref. [43]. The main difference respect to the original HEMAS code is in a more accurate treatment of the muon stochastic energy loss. All the results reported in Section 6 concerning the underground muons are obtained with this propagation program.

6. Results for cosmic ray cascades

In this section we report the results obtained with the shower program in the configurations HEMps, DPMps and DPMdi discussed above. All runs have been performed for vertical primary cosmic rays of fixed mass and energy. The sampling of the on-ground components (electromagnetic shower size and high energy muons

Table 10
List of runs and muon yields above 1 TeV in the three configurations.

Mass	En./nucleon (TeV)	No. of Showers	HEMps	DPMps	DPMdi
1	3	560000	1285	2256	-
56	3	10000	1297	2738	3425
1	10	280000	15363	16301	-
4	10	70000	15209	16127	18190
14	10	20000	15427	16197	19626
28	10	10000	15289	16342	19231
56	10	5000	15232	15931	19962
1	100	56000	36645	35849	-
56	100	1000	35648	35646	-
1	1000	11200	40306	40622	-
56	1000	200	40325	41009	40090
1	10000	1000	19874	21694	-

with $E_\mu > 1$ TeV) corresponds to 2000 m above sea level (this is approximately the height of the EAS-TOP experiment at Gran Sasso [39,41]). The interactions of high energy muons in the atmosphere are neglected. Then, the high energy muons are propagated through 3800 hg/cm^2 of standard rock which is almost equivalent to the vertical rock overburden of Gran Sasso underground laboratory. However, the results reported below are not referred to any particular apparatus – calculations are for infinite sampling areas, both at surface level and underground – because our goal is to prove the reliability of the HEMAS-DPM Monte Carlo and to compare the results obtained with different interaction models. This will also provide us an estimate of the systematic uncertainty in the calculation of cosmic ray showers associated to the interaction model.

In Table 10 we report the list of the runs performed. We simulated proton showers at 3, 10, 100, 1000 and 10^4 TeV. The minimum energy (3 TeV) is related to the rock depth (3800 hg/cm^2): below this energy the efficiency for producing a muon underground is negligible. Then, primary iron showers have been simulated at the same energy per nucleon (except for 10^4 TeV), but with 56 times less statistics. This gives the possibility to compare directly (without any need of normalization) the results obtained at the same energy/nucleon, with different primary masses. For example, the average number of underground muons per nucleon obtained for 280000 primary proton showers at 10 TeV can be compared with the result for 5000 (i.e. 280000/56) iron showers at 560 TeV (i.e. 10 TeV/nucleon). If the pure-superposition model,"ps", is used for the simulation of iron showers, then the results should be identical; instead, if the direct nucleus-air interaction,"di", is performed, the results could be different and the comparison permits to evaluate the effect of a more correct nuclear fragmentation simulation.

This direct comparison cannot be done for the number of muons per nucleus or for the shower size per nucleus. Obviously also the muon charge ratios cannot be compared: for example, an iron shower in the pure-superposition model is the sum of 28 proton and 28 neutron showers. For the sake of completeness, at 10 TeV per nucleon, we performed also runs of primary helium, nitrogen and magnesium nuclei. This choice is connected to the larger abundance of these elements among the cosmic rays, but HEMASDPM can treat any primary nucleus with mass number 1–56.

Before entering into a detailed summary of results, we think that it can be instructive to follow the main steps of the history of a single shower in atmosphere as obtained by our model. We take as an example a shower induced by a primary iron nucleus with an energy of 3 TeV/nucleon. It is extremely difficult to represent pictorially all the produced particles, so that we concentrate on the branch which follows the nuclear fragmentation. This is reported in Fig. 11; only the particles above the energy threshold (1 TeV) are evidentiated, together with the atmospheric depth (and the corresponding vertical height above the sea level), at each relevant

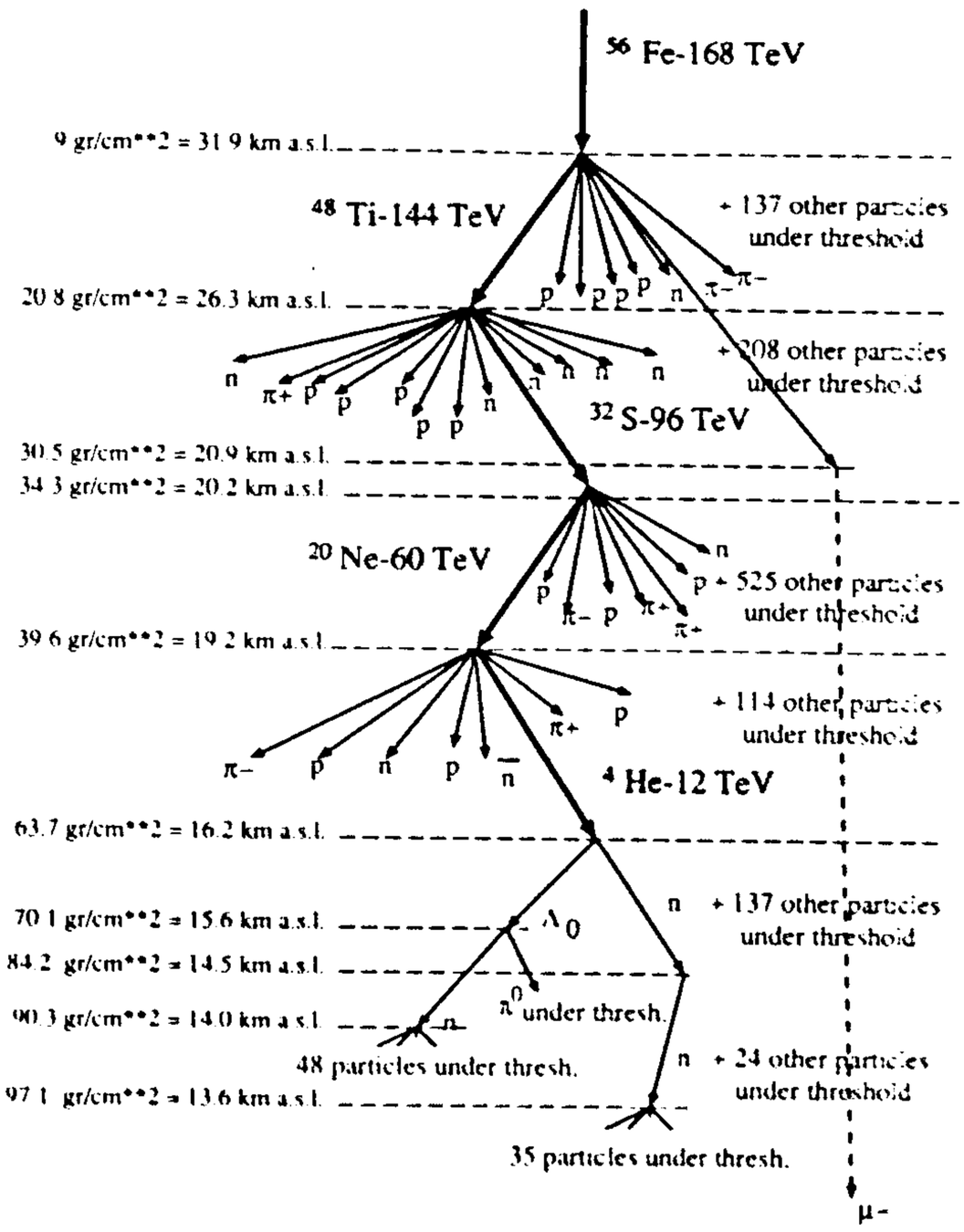

Fig. 11. History of a shower initiated by an iron nucleus with 3 TeV/nucleon. The nuclear fragmentation branch only is followed in detail. At each interaction point only particles produced with an energy above the threshold (E_{thr} = 1 TeV) are represented.

interaction of the considered branch. This shower will produce one muon above threshold, from the decay of a π^- produced in the first interaction.

In the following we summarise the results concerning: the electromagnetic shower size, the muon yield for $E_\mu > 1$ TeV in atmosphere, and the main features of the muons survived underground. We concentrate ourselves on the results obtained using the DPMJET interaction model, and whenever we consider it as important, we quote the comparison with the results obtained when using HEMAS.

6.1. Electromagnetic size of the shower

The electromagnetic size of the shower is the total number of gammas, electrons and positrons. The shower is sampled at 2000 m above the sea level, for an infinite area detector. Fig. 12 shows the average value of the logarithm of the shower size as a function of the primary energy per nucleon. Lower symbols are referred to proton showers. The comparison is between the HEMps and DPMps models (for primary protons the distinction ps/di is not relevant). Even though DPMps provides a size systematically smaller than HEMps, the difference is very small. This is probably due to the fact that the size (including the low energy electromagnetic particles) depends mainly on the correct energy conservation in the interaction, which is guaranteed by both models. The upper symbols in Fig. 12 are for iron showers at 10 100 and 1000 TeV/nucleon for the configurations DPMps and DPMdi. We do not find any significant difference between the results with the pure-superposition model and the results with the direct nucleus–air interaction even though the cross sections used in these models are remarkably different (in the "ps" model the p–air cross section is used while in the "di" model, the nuclear cross sections are used).

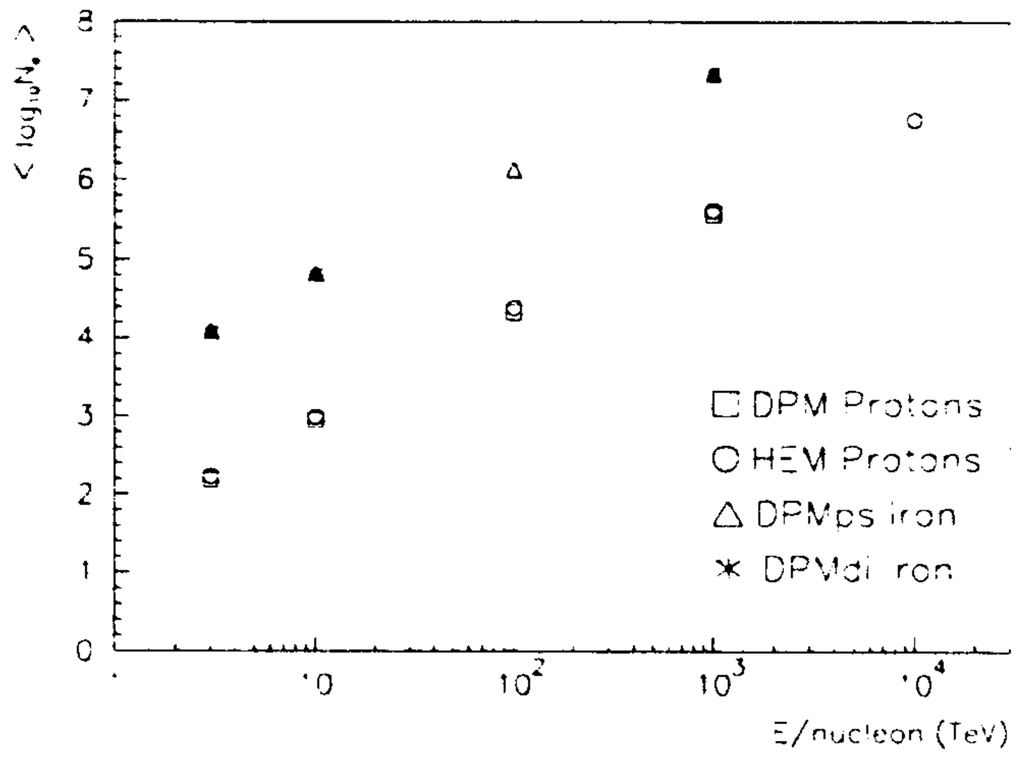

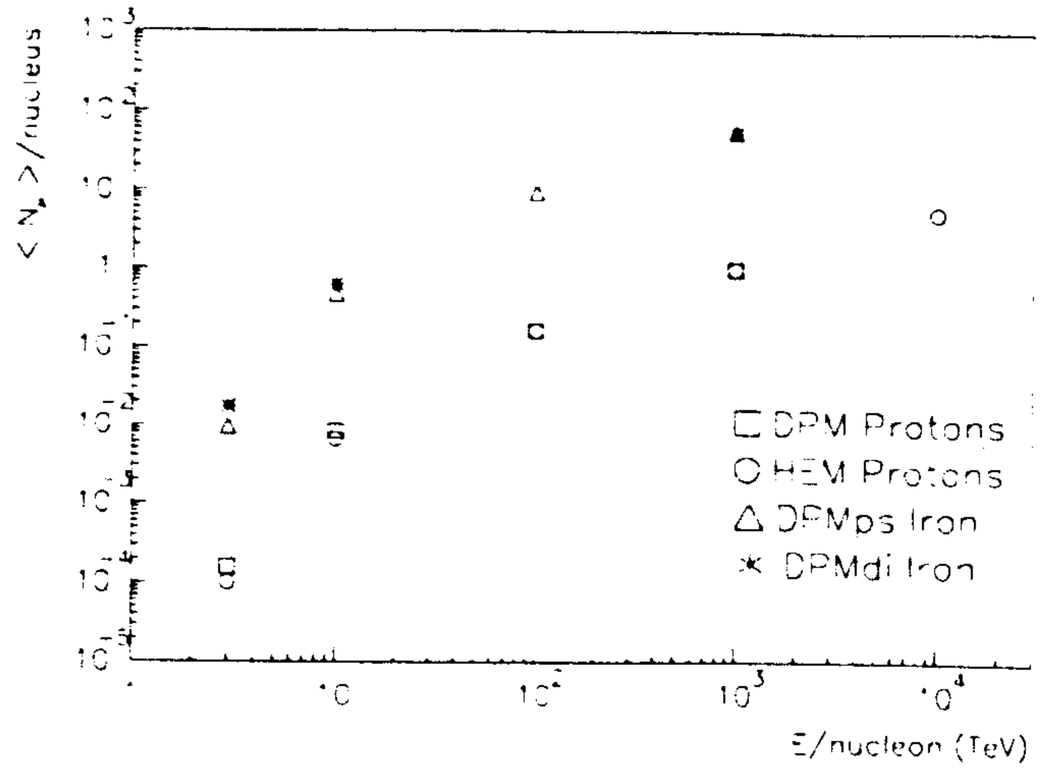

Fig. 12. Mean decimal logarithm of the electromagnetic shower size as a function of the primary energy/nucleon. For proton showers HEMAS and DPMJET are compared. For iron showers, the comparison is between the "ps" and "di" configurations of DPMJET. Here the size per nucleus is considered.

Fig. 13. Average number of underground muons per shower as a function of the primary energy/nucleon. For proton showers HEMAS and DPMJET are compared. For iron showers, the comparison is between the "ps" and "di" configurations of DPMJET.

6.2. *High energy muon yield*

In our simulation run we record the number of atmospheric muons with energy greater than 1 TeV. This quantity is very interesting since it allows also the comparison of our results with the existing analytical calculations. In Table 10 we report the total number of muons obtained in the Monte Carlo runs for the different configurations. In the same table we summarise the number of showers generated for each primary mass. It is interesting to notice how the production of muons with $E_\mu > 1$ TeV increases, in the lowest region of energy/nucleon, when moving from the superposition model to the direct interaction, and also from HEMps to DPMps. However we wish to stress here that the "di" model can still be subject to further refinements in the future, and some results might change.

6.3. *Underground muons*

The number and the characteristics of underground muons depend on the primary cosmic ray mass, energy, zenith angle and on the rock depth. In our calculations the last two are fixed, because we want to focus on the energy and mass dependence. In this section we discuss muon multiplicity, their history in the shower, in particular the kinematical variables of their parents. We derive their lateral distribution function, and we also give some preliminary results about the prompt muon production.

6.3.1. *Average multiplicity*

In Fig. 13 we show the average number of underground muons per shower as a function of the energy per nucleon of the primary. The results for proton showers (lower symbols) show that DPMJET provides a larger $\langle N_\mu \rangle$/nucleus than HEMAS, especially at low proton energy. This is shown in another form in the Fig. 14, where the stars represent the ratio $\langle N_\mu \rangle_{DPM}/\langle N_\mu \rangle_{HEM}$ for proton showers (this can be considered a correction factor to be applied to the parametrisation of $\langle N_\mu \rangle$ in Ref. [35] to calculate the $\langle N_\mu \rangle$ value as obtained in DPMJET. We remind that at the considered rock depth, the total muon rate is mainly due to protons (and also helium nuclei) in the total energy range $3 < E < 100$ TeV, so we expect DPMJET to predict more single muons than HEMAS for the same primary proton flux. This could be also predicted by examining the comparative

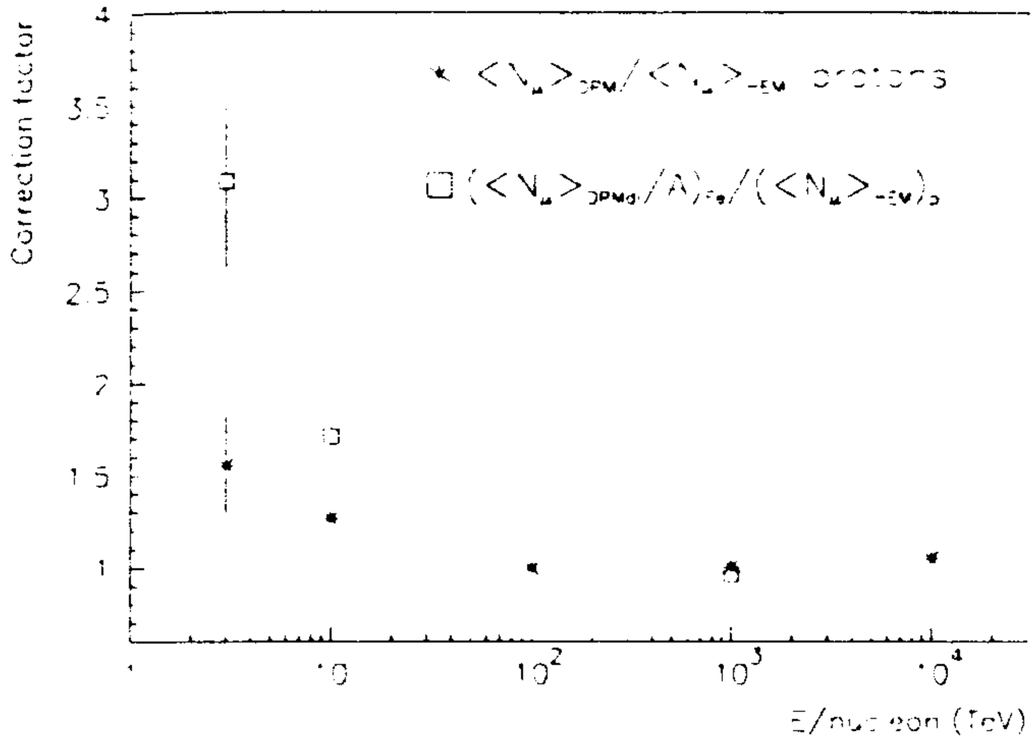

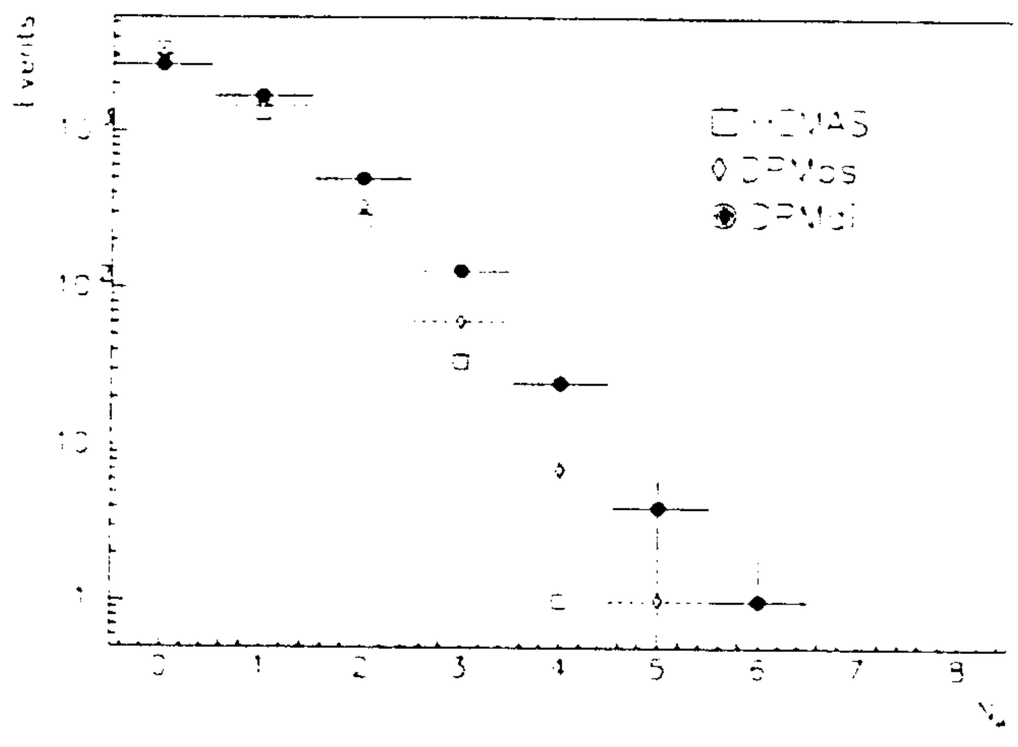

Fig. 14. Correction factors to be applied to the HEMAS result for the average number of underground muons in proton showers to obtain the DPMJET value for proton and iron showers. In the case of iron, the number of muons per nucleon is considered.

Fig. 15. Distribution of the underground muon multiplicity for primary vertical iron nuclei of 560 TeV for HEMps, DPMdi and DPMps. Rock depth is 3800 hg/cm^2.

behaviour of Z functions, reported in Table 8. Looking back at Fig. 13, the upper symbols correspond to the calculations for iron showers with DPMJET. The "ps" results are (within statistical errors) 56 times the $\langle N_\mu \rangle$ for protons (squares). The results for direct interaction are above the "ps" values at low energy/nucleon. This is not surprising, at least because the iron path length in air is much smaller than the proton one (which is used in the "ps" context). As a consequence, the shower develops higher in the atmosphere and the probability for high energy pions to decay is larger. This is shown again in Fig. 14, where the squares represent the ratio between the average number of muons per nucleon $\langle N\mu \rangle/56$ for iron showers with DPMdi and the average number of muons for proton showers with HEMps (at the same energy per nucleon). The effect of the realistic nuclear interaction treatment is evident at low energy.

It is also interesting to examine the muon multiplicity distribution for a fixed primary mass and energy. As an example, in Fig. 15 we show the distribution of N_μ for primary (vertical) iron nuclei, at 10 TeV/nucleon, as obtained with DPMdi and DPMps at the depth of 3800 hg/cm^2 compared to the result achieved with HEMAS. Of course there is a strong dependence of the parameters characterising such distributions upon the rock depth (which in practice is equivalent to an energy threshold), shower angle, etc., as discussed in Ref. [35].

In Fig. 16 we compare the distribution of the vertical production height H (as measured from the sea level) of the underground muons of Fig. 15 obtained with DPMdi and DPMps: in the "di" case $\langle H \rangle$ is larger.

6.3.2. Kind of muon grandparent

Usually, when a calculation on underground muons is performed, much attention is spent on the correct proton–air simulation. The same effort has to be devoted to the study of hadron–air interactions for hadrons different from protons. This is made more difficult by the poor amount of data for non-proton interactions. As a first approximation, the high energy muons are believed to be produced mainly in the sequence: proton+air $\rightarrow \pi$ or $K \rightarrow \mu$ (in this case we define muon parent the π or the K, while the proton is the muon grandparent). This is only partially true: in proton showers at 3 TeV, 95% of the muon grandparents are nucleons; this percentage decreases down to 40% at 1000 TeV; in this latter case up to 39% of the grandparents are pions. Thus, at high energy a correct simulation of non-proton interactions is very important.

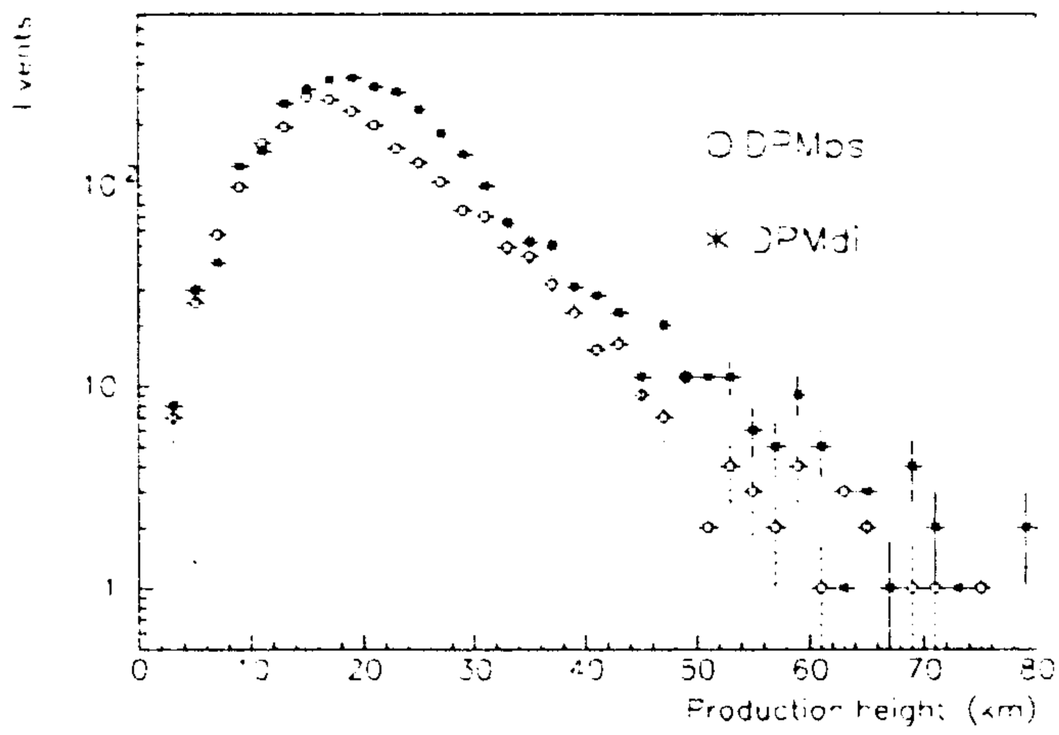

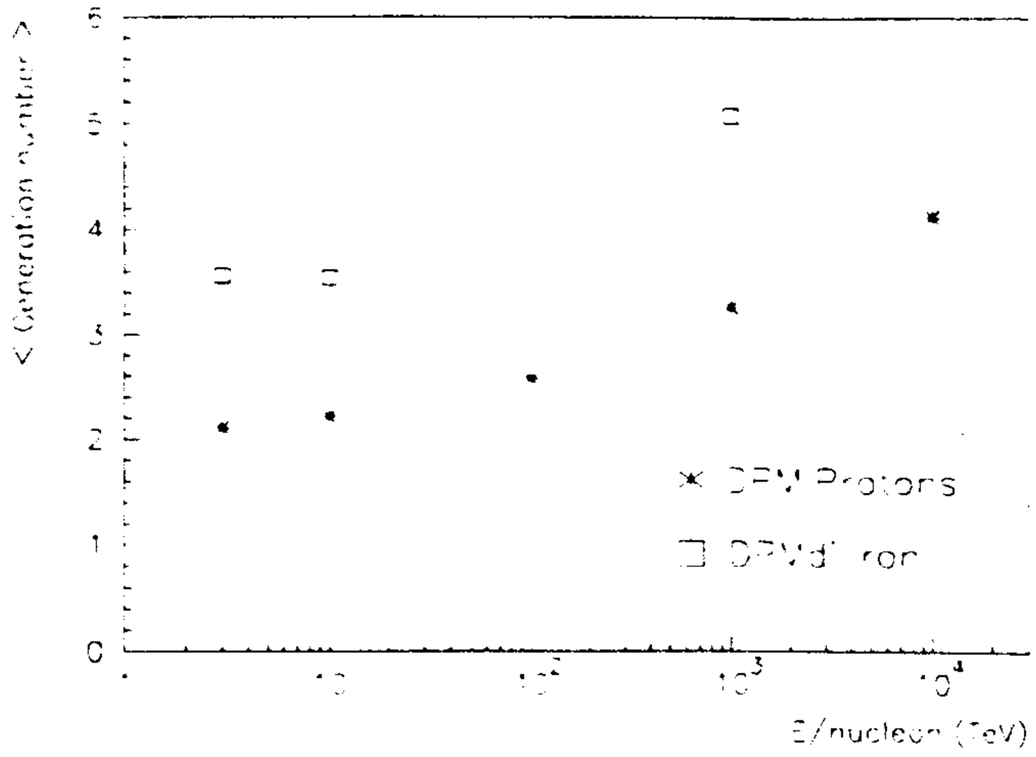

Fig. 16. Distribution of the production height of underground muons for primary vertical iron nuclei of 560 TeV. Rock depth is 3800 hg/cm^2. The average heights turn out to be 20.35 km (ps) and 21.76 km (di).

Fig. 17. Mean generation number of underground muons as a function of primary energy per nucleon. The simulation of the "direct interaction" of nuclei provide larger values of the generation number with respect to proton showers (or to a "pure superposition" model).

6.3.3. Muon generation

The results about the muon grandparent are also visible in the so-called muon generation number G. We define the generation number of a particle in the shower as follows: the primary has $G = 0$; the particles produced in its first interaction have $G = 1$. Then G increases by one for each successive interaction or decay in the shower, except for the production of prompt mesons which decay directly at the level of the interaction routine (DPMJET-II only), and thus do not cause an increment in the generation number. For example, a muon can have generation number 1 if it is produced promptly in the first primary interaction: primary $(G = 0) \rightarrow D(G = 0) \rightarrow \mu_{prompt}(G = 1)$, where the D meson does not appear in the shower history. In proton showers, most of the muons have $G = 2$ (i.e. they come from a π or K produced in the first primary interaction). However, the fraction of underground muons with $G = 2$ decreases with the primary energy (89.4% at 3 TeV, down to 27.4% at 1000 TeV). This confirms the above considerations on the muon grandparent.

If the primary is a nucleus with $A > 1$, and a realistic fragmentation model is adopted (like DPMdi), then the generation numbers change drastically because the nucleus is fragmented in many successive interactions (in each interaction G is incremented). In low-energy (3–10 TeV/nucleon) iron showers, about 40% of the underground muons have $G > 3$, and this percentage increases up to 75% at high energy (1000 TeV/nucleon). In Fig. 17 we show the average muon generation number $\langle G \rangle$ as a function of the energy per nucleon. Both effects – the increase of $\langle G \rangle$ with energy and the larger $\langle G \rangle$ value in heavy primary showers – are evident.

6.3.4. Kind of muon parent

In this paragraph we do not yet discuss prompt muons, therefore the muon parent can be only a charged pion or a kaon ($K^{\pm}$ or K_0^L). The fraction of muons coming from K_0^L is very small: for proton showers, with DPMJET, it increases with the primary energy up to 0.7% at 10^4 TeV. On the contrary, the contribution of charged kaons is quite relevant: the ratio between the number of muons coming from kaons ($K^{\pm} + K_0^L$) with respect to those coming from pions increases from 0.21 at 3 TeV up to 0.39 at 10^4 TeV in proton showers. These results are shown in Fig. 18, together with the calculation for iron showers with DPMdi. The increasing contribution of K mesons is a consequence of both the increasing interaction probability of pions, and the increasing contribution in the model by the strange sea quarks (see Section 2.2.3).

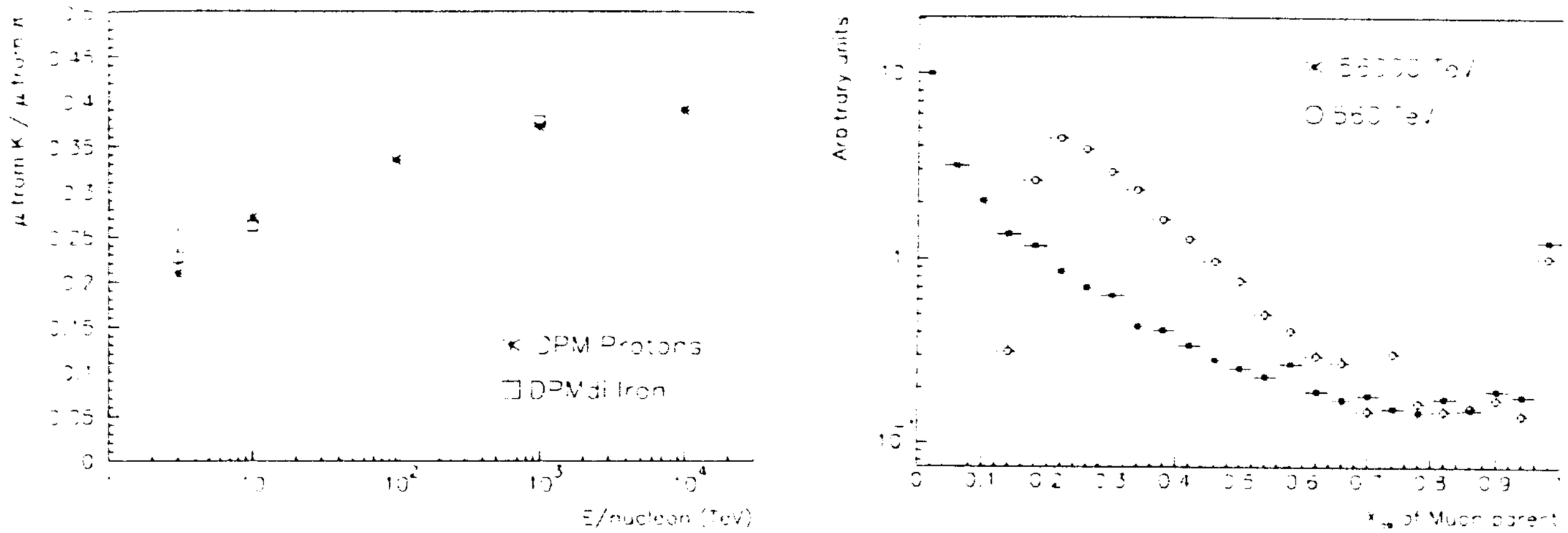

Fig. 18. Ratio between the number of underground muons with a parent kaon respect to those with a parent pion, as a function of the primary energy/nucleon.

Fig. 19. Distribution of the underground muon parent fractional energy. The results for DPMdi at 560 and 56000 TeV are compared (the curves are normalized to the same area).

The realistic simulation of the nuclear interaction ("di") does not change evidently the kaon contribution to the underground muon production.

6.3.5. x_L of the muon parent

One of the most important features of hadron–air interactions concerning the high energy muon production, is the Feynman x_F distribution of pions and kaons (possible muon parents) in the projectile fragmentation region. In HEMAS-DPM we store the fractional energy of the muon parent with respect to its grandparent in the laboratory frame x_L. This variable is practically identical to the Feynman x_F, at high energy and in the projectile fragmentation region. The x_L distribution will tell us what is the relevant x_F region in hadron–air interaction for the production of high energy muons detected underground. Let us define x_L^{thr} as the ratio of the minimum muon energy required to transverse the rock depth considered and the primary energy per nucleon. We can thus predict that the important x region depends crucially on the primary energy, especially when x_L^{thr} is not close to zero. This emerges in the following discussion. In Fig. 19 we show the x_L distribution of the underground muon parents for iron showers at 10 and 1000 TeV/nucleon with DPMdi. The contribution of diffractive pion–air and K–air interactions to the underground muon production is evidenced by the peak near $x_L = 1$. We verified that the fraction of muons coming from a parent with $x_L > 0.90$ is smaller than 6.2% in the complete set of runs performed. In the same figure we also notice that the bulk of the muons have a parent with x_L between the threshold value x_L^{thr} and about 0.4–0.5. The region $0.5 < x_L < 0.9$ seems to be marginally relevant for the high energy underground muon production. However, if we look at the analogous distribution at 3 TeV per nucleon, we find that the relevant region is 0.5–0.9, plus a small contribution of diffraction. This is shown clearly in Fig. 20, where we plot the average x_L of the muon parents as a function of primary energy. At low energy (around 3 TeV) x_L^{thr} is far from zero and the extreme fragmentation region provides the bulk of the muons. As the primary energy increases, $\langle x_L \rangle$ tends to an almost constant value (0.18 at 100 TeV, 0.19 at 1000 TeV, 0.21 at 10^4 TeV). This point deserves however a deeper discussion, since the energy spectrum of primary cosmic rays behaves like a steep falling power law, so that one could be brought to conclude that the high x range would be in any case dominant. We stress here that this is not the case. In fact, one has to remind that whenever the primary energy is close to the muon energy threshold, the muon yield is very small. See Fig. 13. We notice how $\langle N_\mu \rangle$ drastically increases with energy in the region just above the muon energy threshold:

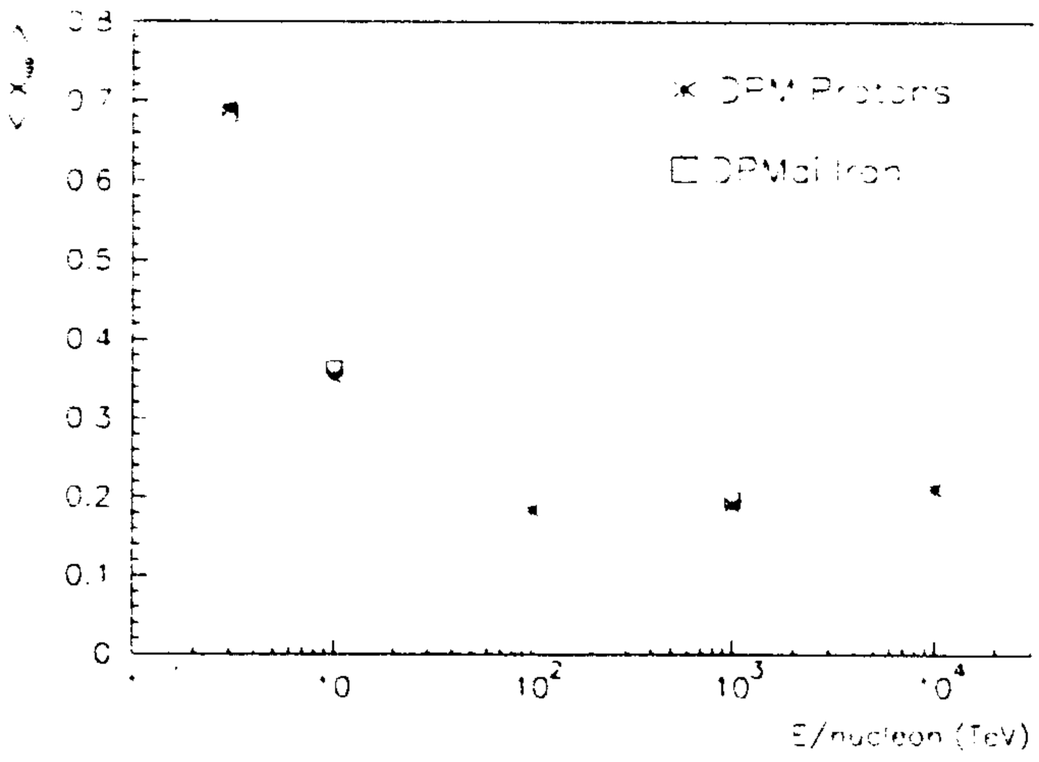

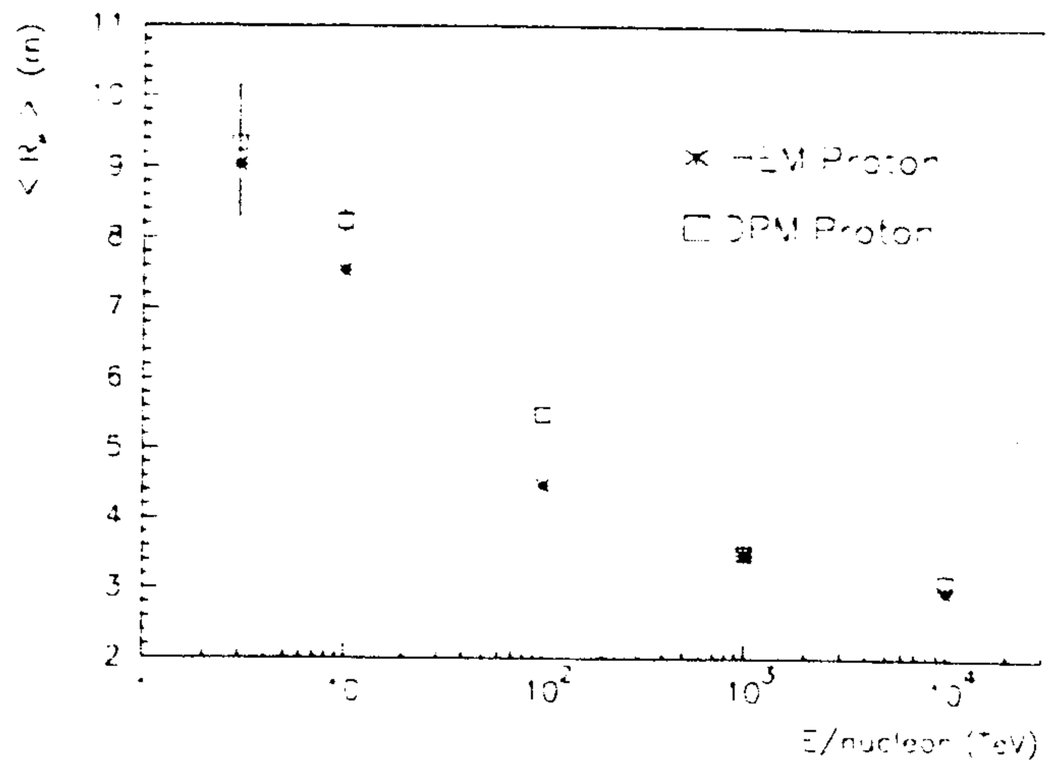

Fig. 20. Average fractional laboratory energy of underground muon parents as a function of the primary energy/nucleon.

Fig. 21. Average distance from shower axis for underground muons as a function of the primary energy/nucleon. The results of HEMAS and DPMJET are compared for primary protons.

between 3 and 10 TeV/nucleon (N_μ) increases by almost two orders of magnitude. Such an effect can cancel and even invert the weight of the low energy region of primary spectrum. In practice, for a given experimental situation, the high energy muon inclusive features (including the x of the parent) are mostly determined by primary particles with an energy/nucleon about 10 times larger than the muon energy threshold. Therefore we believe that the region $x < 0.5$ remains the dominant one, even when we perform the integration over the whole energy spectrum and all possible arrival directions (and consequently, over all possible rock depth values).

6.3.6. Muon lateral displacement

The muon lateral displacement (i.e. the distance from the shower axis) depends on many features of the interaction model: the cross sections, which determine the muon production height, the pion (or kaon) transverse momentum and Feynman X, which determine the muon angle respect to the shower axis. Therefore, when the interaction model is modified or completely changed, the effects on the displacement R_μ are hardly predictable. We remind here that R_μ is defined by the muon distance from the shower axis, as measured in a plane orthogonal to the direction of the shower, at a given depth (in our case at 3800 hg/cm^2 of standard rock, in the vertical direction). In Fig. 21 we show the average spread $\langle R_\mu \rangle$ for proton showers as a function of the proton energy for the HEMAS and the DPMJET models. We notice that DPMJET predicts larger values of $\langle R_\mu \rangle$. In Fig. 22 we show the behaviour of $\langle R_\mu \rangle$ as a function of energy/nucleon for primary Iron nuclei as obtained with HEMAS-DPM in the "di" and "ps" configuration. Here also we compare the shape of R_μ distributions as obtained with the different models. In Fig. 23 the distribution shapes obtained with DPMJET and HEMAS are compared for iron nuclei at 10 TeV/nucleon, while in Fig. 24 they are compared for the same nuclei at 1000 TeV/nucleon. The differences with respect to HEMAS are more evident in the lower energy range, and in the "di" case. As an example, in Fig. 25 we plot the ratios between the distributions obtained in the case of 560 TeV iron nuclei.

As discussed in Ref. [35], the rock depth and the direction strongly affect such a distribution: at higher energy (larger rock depth) muons have the tendency to be nearer. The higher is the angle, the higher is the average production height of muon parents, and thus larger is the muon lateral displacement.

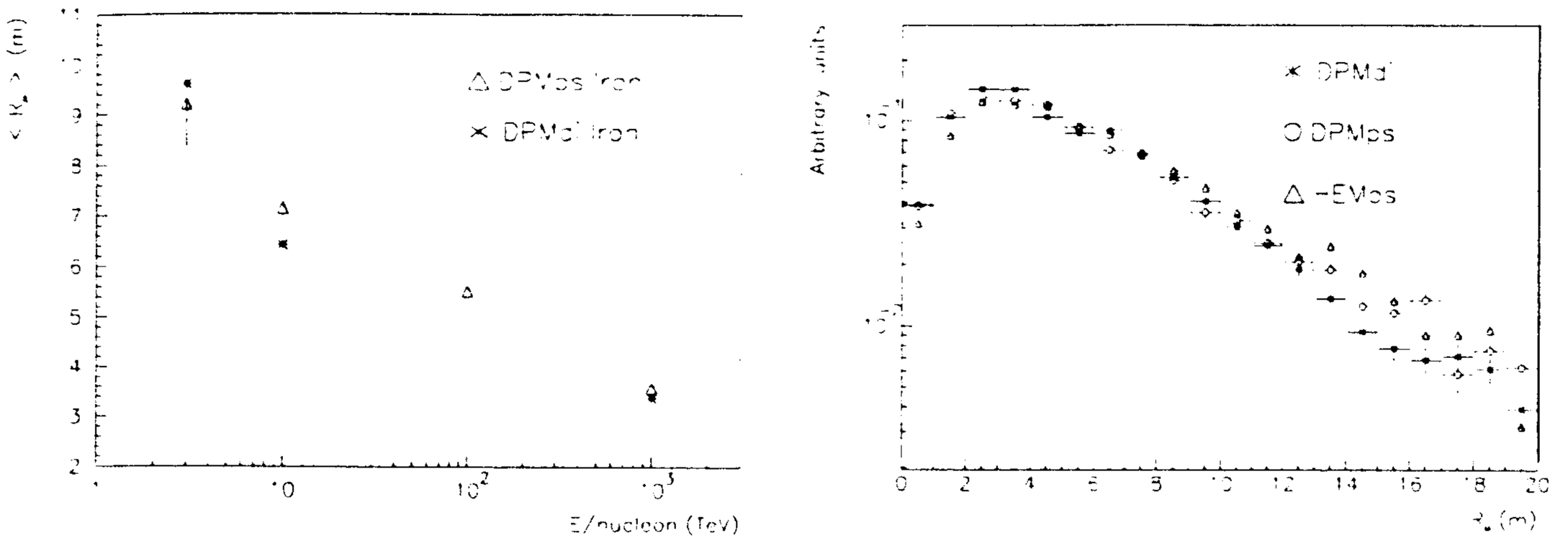

Fig. 22. Average distance from shower axis for underground muons as a function of the primary energy/nucleon. The results of DPMps and DPMdi are compared for primary iron nuclei.

Fig. 23. Distribution of the underground muon distance from shower axis for primary iron nuclei of 560 TeV. Curves are normalized at the same area.

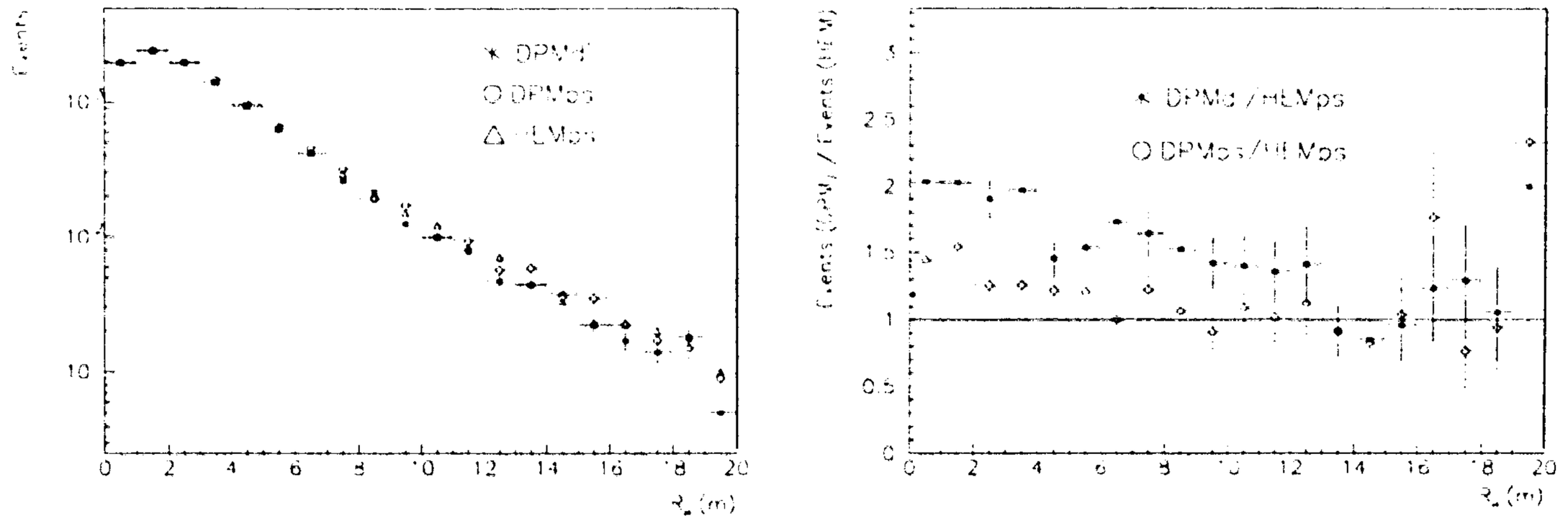

Fig. 24. Distribution of the underground muon distance from shower axis for primary iron nuclei of 56000 TeV. Curves are not normalized.

Fig. 25. Ratios between the distributions of the underground muon distance from shower axis provided by DPMJET for primary iron nuclei of 560 TeV and the corresponding curve for HEMAS. Curves were not normalized before the calculation of the ratios. A line is drawn in correspondance of unit ratio.

6.3.7. *Prompt muons*

As anticipated earlier, in this paper we do not make a detailed study of the prompt muon component. This calculation requires a better study of the heavy flavor production in our model and a much higher statistics at simulation level. This will be discussed in detail in a following paper. We include this topic in this paper only to indicate that DPMJET in the future will be capable in predicting the production of prompt muons. As a preliminary result, in Table 11 we report the number of prompt muons obtained in each run, in atmosphere (with $E_\mu > 1$ TeV) and underground. As an example, we shall consider the case with more statistics: 11200 proton showers of 1000 TeV provide: 30 prompt muons over a total of 40622 in atmosphere; 16 prompt muons over a total of 11161 underground. For a reason of statistics, we consider only the atmospheric muons. The prompt

Table 11
Comparison between the number of prompt muons (Pro) and the total number of muons (All) for high energy (> 1 TeV) atmospheric muons (ATM) and for underground muons (UND). Calculations are with the DPMJET model (DPMdi for $A > 1$ nuclei). The 24 prompt ATM muons for Iron of 1000 TeV/nucleon are 22 single muon and one double muon events.

Mass	En./nucleon (TeV)	No. of Showers	Pro ATM	Pro UND	All ATM	All UND
1	3	560000	0	0	2256	104
56	3	10000	0	0	3425	173
1	10	280000	0	0	16301	2381
4	10	70000	0	0	18190	2832
14	10	20000	1	0	19626	3042
28	10	10000	0	0	19231	2940
56	10	5000	1	0	19962	3176
1	100	56000	10	7	35849	9310
1	1000	11200	30	16	40622	11161
56	1000	200	24	13	40090	10704
1	10000	1000	13	4	21694	5602

muons are mostly produced in the decay of charged mesons generated in hadron (nucleus)–air interactions. These 30 prompt muons derive from: 22 nucleon–air, 6 $\pi^{\pm}$–air and 2 antinucleon–air interactions. Thus, the major part of the prompt muons come from an interaction of a very energetic particle (in proton showers the most energetic particles are the leading nucleons). The average generation number of these 30 prompt muons is $\langle G \rangle = 1.70 \pm 0.16$ to be compared with $\langle G \rangle = 3.56$ of the all-muon set. It is evident that most of the prompt muons are produced in the first primary interaction (primary $G = 0 \rightarrow D$ meson $G = 0 \rightarrow$ prompt μ $G = 1$) or in the second generation (primary $G = 0 \rightarrow$ hadron $G = 1 \rightarrow D$ meson $G = 1 \rightarrow$ prompt μ $G = 2$). The prompt muons are produced with a transverse momentum larger than the $p_\perp$ of non-prompt muons: $\langle p_\perp \rangle = 0.79 \pm 0.09$ GeV, to be compared with $\langle p_\perp \rangle = 0.45$ GeV for the all-muon sample (here the $p_\perp$ is referred to the primary direction, not to the parent direction). This is due to the fact that the D mesons are produced with an average $p_\perp$ larger than that of pions and kaons. As far as the energy is concerned, the prompt muons have a larger average energy than the non-prompt muons: $\langle E_\mu \rangle = 6.66 \pm 1.67$ TeV, to be compared with $\langle E_\mu \rangle = 2.35$ TeV for the all-muon sample (we remind that only muons above 1 TeV in atmosphere are considered). This is perfectly consistent with the considerations on the G number. As already discussed above, the muon lateral displacement depends on many factors: the muon angle with respect to the shower axis (approximately given by $p_\perp/E_\mu$) and the slant distance traveled by the muon from the production point down to the atmospheric sampling level. For prompt muons we have, with respect to the non-prompt ones: larger $p_\perp$, much larger energy (thus a smaller angle $p_\perp/E_\mu$) but also a larger production height H. Therefore, it is not easy to predict the effect on $\langle R_\mu \rangle \sim (\langle p_\perp \rangle / \langle E_\mu \rangle) \cdot \langle H \rangle$. We obtained: $\langle R_\mu \rangle = 5.25 \pm 0.94$ m for prompt muons and $\langle R_\mu \rangle = 4.18$ m for the all-muon sample. Although the first value is larger than the second one, the statistical uncertainty does not yet allow to draw any firm conclusion.

7. Summary

The event generator DPMJET-II based on the dual parton model has become a valid alternative to models like HEMAS [35], and SIBYLL [31] to simulate the high energy hadron–hadron, hadron–nucleus and nucleus–nucleus collisions within a cosmic ray cascade code.

The excellent Feynman scaling found with DPMJET in large parts of the x_F-region in hadron–hadron and hadron–nucleus collisions gives us the confidence that accelerator data on Feynman x_F-distributions in the projectile fragmentation region are indeed very relevant for applications in the cosmic ray energy region.

The model provides hadron–hadron total, inelastic, elastic and diffractive cross sections consistent with accelerator data. The hadron–air cross sections derived from this are consistent with hadron–air cross sections extracted from cosmic ray experiments. The model provides also all the necessary cross sections to study nucleus–nucleus collisions in the cosmic ray cascade.

As a consequence from the excellent Feynman scaling in the model, we find spectrum-weighted moments Z_π and Z_K, for hadron-air collisions, which remain rather constant with increasing collision energy, in contrast to the behaviour of other models, where these moments decrease more strongly with energy. These moments for h–air collisions are however smaller than the corresponding moments in hadron–hadron collisions.

The fraction of the primary energy carried by the leading particles in the collision decreases with energy and with the mass of the target nuclei. A large part of this decrease is due to the decreasing fraction of diffractive (single diffractive and double diffractive) events with rising energy and rising target mass.

The model incorporates the Cronin effect and shows a strong seagull effect. Correspondingly the average transverse momenta $\langle p_\perp \rangle$ rise with the collision energy (mainly due to the rise of the minijet production cross section), with the mass of the nuclear target and projectile and with rising Feynman x_F.

It is important that the model is able to give a good description of hadron production in nucleus–nucleus collisions. Due to the large fraction of nuclei in primary cosmic rays, nucleus–air collisions are of great importance in the cosmic ray cascade. It has been shown that these collisions in the dual parton model differ considerably from what is expected in simple approximations like different superposition models.

We observe, in agreement to what is known from accelerator experiments, a significant enhancement of strange hadron production with the collision energy, with the transverse momentum, with the secondary multiplicity of the collision and with the mass of the nuclear projectiles and targets (see also Ref. [2]).

The DPMJET interaction model, when used inside a shower code, provides results very similar to those obtained with other codes, but allows to extend the analyses of present data at high energy, thanks to the possibility to calculate the direct A–A collisions. In fact, interesting features now appear when releasing the simple superposition model, that has been so often used so far in the field of cosmic rays.

This model of direct nucleus–nucleus interaction can be surely improved. This will be the object of our future investigations.

Acknowledgements

One of the authors (J.R.) acknowledges the collaboration with P. Aurenche, F. Bopp, A. Capella, R. Engel, A. Ferrari, H.J. Möhring, C. Pajares, D. Pertermann, S. Roesler, P. Sala and J. Tran Thanh Van on different aspects of the dual parton model; he acknowledges the hospitality of Professor L. Mandelli in Milano and Professor E. Iarocci and Professor M. Spinetti in Frascati, where the presented calculations were performed and he thanks INFN for supporting these studies.

References

[1] A. Capella, U. Sukhatme, C.-I. Tan and J. Tran Thanh Van, Phys. Rep. 236 (1994) 225.
[2] J. Ranft, LNF-94/035 (P), submitted to Phys. Rev. D, 1994.
[3] P. Aurenche, F.W. Bopp, A. Capella, J. Kwiecinski, M. Maire, J. Ranft and J. Tran Thanh Van, Phys. Rev. D 45 (1992) 92.
[4] F.W. Bopp, D. Pertermann, R. Engel and J. Ranft, Phys. Rev. D 49 (1994) 3236.
[5] A. Capella, J. Tran Thanh Van and J. Kwiecinski, Phys. Rev. Lett. 58 (1987) 2015.
[6] F.W. Bopp, D. Pertermann and J. Ranft, Z. Phys. C 54 (1992) 683.
[7] R. Engel, F.W. Bopp, D. Pertermann and J. Ranft, Phys. Rev. D 46 (1992) 5192.
[8] K. Hahn and J. Ranft, Phys. Rev. D 41 (1990) 1463.
[9] A. Capella and J. Tran Thanh Van, Z. Phys. C 10 (1981) 249.
[10] A.B. Kaidalov and O.I. Piskunova, Z. Phys. C 30 (1986) 145.

[11] J. Ranft, Phys. Rev. D 37 (1988) 1842.
[12] H.J. Möhring and J. Ranft, Z. Phys. C 52 (1991) 643.
[13] I. Kawrakow, H.J. Möhring and J. Ranft, Z. Phys. C 56 (1992) 115.
[14] H.J. Möhring, J. Ranft, A. Capella and J. Tran Thanh Van, Phys. Rev. D 47 (1993) 4146.
[15] S. Roesler, R. Engel and J. Ranft, Z. Phys. C 59 (1993) 481.
[16] J. Ranft, A. Capella and J. Tran Thanh Van, Phys. Lett. B 320 (1994) 346.
[17] S.Yu. Shmakov, V.V. Uzhinskii and A.M. Zadoroshny, Comput. Phys. Commun. 54 (1989) 125.
[18] S. Ritter, Comput. Phys. Commun. 31 (1984) 393.
[19] J. Ranft and S. Ritter, Acta Phys. Pol. B 11 (1980) 259.
[20] K. Hänssgen and S. Ritter, Comput. Phys. Commun. 31 (1984) 411.
[21] T. Sjöstrand, CERN Report CERN-TH.6488/92 (1992).
[22] J.W. Cronin et al., Phys. Rev. D 11 (1975) 3105.
[23] S. Roesler and J.Ranft, Z. Phys. (1993).
[24] M. Gazdzicki and O. Hansen, Nucl. Phys. A 528 (1991) 754.
[25] M. Adamus et al., EHS-NA22 Collaboration, Z. Phys. C 39 (1988) 311.
[26] D.S. Barton et al., Phys. Rev. D 27 (1983) 2580.
[27] D.A. Garbutt et al., Phys. Lett. B 67 (1977) 355.
[28] T.K. Gaisser, Cosmic Rays and Particle Physics (Cambridge University Press, Cambridge, 1992).
[29] J. Durand and H. Pi, Phys. Rev. Lett. 58 (1987) 2015.
[30] T.K. Gaisser and F. Halzen, Phys. Rev. Lett. 54 (1987) 1754.
[31] R.S. Fletcher, T.K. Gaisser, P. Lipari and T. Stanev, Bartol preprint BA 94-01, submitted to Phys. Rev. D, 1994.
[32] X.N. Wang and M. Gyulassy, Phys. Rev. D 44 (1991) 3501.
[33] A.D. Martin, R.G. Roberts and W.J. Stirling, Phys. Rev. D 47 (1993) 867.
[34] H.-C.T. Abt et al., DESY preprint DESY 93-117, submitted to Nucl. Phys. B, 1993.
[35] C. Forti, H. Bilokon, B. d'Ettorre Piazzoli, T.K. Gaisser, L. Satta and T. Stanev, Phys. Rev. D 42 (1990) 3668.
[36] E. Gotsman, E.M. Levin and U. Maor, Phys. Rev. D 49 (1994) 4321.
[37] The MACRO Collaboration (S.P. Ahlen et al.), Phys. Lett. B 249 (1990) 149.
[38] The MACRO Collaboration (S.P. Ahlen et al.), Phys. Rev. D 46 (1992) 895.
[39] The EAS-TOP and MACRO Collaborations (M. Aglietta et al.), Proc. 23rd ICRC, Calgary 2 (1993) 89.
[40] The MACRO Collaboration (S.P. Ahlen et al.), Phys. Rev. D 46 (1992) 4836.
[41] The EAS-TOP and MACRO Collaborations (M. Aglietta et al.), Phys. Lett. B 337 (1994) 376.
[42] J. Engel, T.K. Gaisser, P. Lipari and T. Stanev, Phys. Rev. D 46 (1992) 5013.
[43] P. Lipari and T. Stanev, Phys. Rev. D 44 (1991) 3543.
[44] A. Fásso et al., Fluka: present status and future developments, IV Int. Conf. on Calorimetry in High Energy Physics, La Biodola (Is. d'Elba), Italy, 1993.
[45] P.A. Aarnio and M. Hutinen, Proceedings MC93, Int. Conf. on Monte Carlo Simulation in High Energy and Nuclear Physics, Tallahassee, USA, 1993.
[46] R. Brun et al., CERN DD/E/84-1 (1984).
[47] V. Patera, M. Carboni, G. Battistoni and A. Ferrari, LNF-94/015 (P), submitted to Nucl. Instr. Meth., 1994.
[48] J.L. Bailly et al., EHS-RCBC-Collaboration, Z. Phys. C 35 (1987) 295.
[49] H.H. Mielke, M. Föller, J. Engler and J. Knapp, J. Phys. G 20 (1994) 637.